Fall 8-2022

Fermion-induced Electroweak Symmetry Non-restoration via Temperature-dependent Masses

Yu Hang Ng
University of Nebraska-Lincoln, yu-hang.ng@huskers.unl.edu

FERMION-INDUCED ELECTROWEAK SYMMETRY NON-RESTORATION VIA TEMPERATURE-DEPENDENT MASSES

by

Yu Hang Ng

A DISSERTATION

Presented to the Faculty of
The Graduate College at the University of Nebraska
In Partial Fulfilment of Requirements
For the Degree of Doctor of Philosophy

Major: Physics and Astronomy

Under the Supervision of Professor Peisi Huang

Lincoln, Nebraska
August, 2022

FERMION-INDUCED ELECTROWEAK SYMMETRY NON-RESTORATION VIA TEMPERATURE-DEPENDENT MASSES

Yu Hang Ng, Ph.D.

University of Nebraska, 2022

Advisor: Peisi Huang

Standard Model (SM) and many extensions of SM predict that the electroweak (EW) symmetry was restored in the early universe when the temperature was around 160 GeV. However, recent studies showed that the interactions between some new scalars and $SU(2)_L$ Higgs doublet(s) can cause the EW symmetry to remain broken at temperatures well above the EW scale in certain renormalizable extensions of SM. In this study, we found that new fermions from renormalizable models can also induce this EW symmetry non-restoration effect, provided that they have the appropriate temperature-dependent masses. These masses can arise naturally from the interactions between the new fermions and scalar fields. After introducing these models, I will explain how the important higher-order corrections are handled in the calculations of effective potentials. There are also theoretical and experimental constraints that must be taken into account. Within the allowed parameter space, I will examine the characteristics of the novel thermal histories predicted by these models. Certain cases predict that the EW phase transitions are strongly first-order and occur at temperatures much higher than the EW scale. I will discuss the prospect of detecting the stochastic gravitational-wave background from these cosmological phase transitions at future gravitational wave observatories, such as BBO and DECIGO.

Acknowledgements

I would first like to express my deepest gratitude to my advisor, Prof. Peisi Huang. This thesis work would not have been possible without her guidance. She is a very caring mentor and is always available for research discussions. I also very much appreciate her helpful advice and honest opinions. Although I did not always agree with her, she made me feel comfortable expressing my disagreements and taught me how to analyze complex problems from multiple perspectives. I am very fortunate to have Peisi suggested this research project to me. From this project, I have learned about various interesting topics, including finite-temperature quantum field theory, renormalization-group improved effective potential of multi-scale models, cosmological phase transitions, and gravitational waves. I have had a lot of fun exploring the connections between particle physics and early-universe cosmology.

I would like to extend my sincere thanks to Dr. Graham A. White for several fruitful discussions. His suggestions allowed me to explore larger classes of temperature-dependent mass models with novel electroweak phase structures. I am also very grateful to Prof. Kenneth Bloom, Prof. Bradley Shadwick, and Prof. Susan Hermiller for serving on my doctoral supervisory committee. Many thanks to Prof. Kenneth Bloom and Prof. Bradley Shadwick for their evaluation of my dissertation and thesis defense and valuable comments.

In my Ph.D. journey, I received a lot of help from many people, and I would like to thank them all. Special thanks to my good friends, Xiaojun Wang and Tianlin Li, for their unlimited support and sincere attitudes.

Lastly, there are no words to express my gratitude to my family for their unconditional love.

Table of Contents

List of Figures

List of Tables

Chapter 1

Introduction

In 1970s, Kirzhnits and Linde first suggested that the electroweak symmetry would be restored in the early universe when the temperature is sufficiently high [1]. Weinberg later derived the formalism that can be used to calculate the critical temperatures for general renormalizable field theories with global or gauge symmetries, which now became the foundation of finite-temperature quantum field theory [2]. In the Standard Model (SM), the electroweak phase transition (EWPT) occurs at $T_c = 159.5 \pm 1.5$ GeV and it is a smooth cross-over [3–7]. At present, the exact nature of EWPT is not clear because the shape of Higgs potential has not been measured precisely enough. The nature of EWPT and the evolution of Higgs potential in the early universe certainly are important questions to study in their own right, the intimate relationship between the electroweak symmetry and the violation of baryon and lepton number make these issue even more critical as they may lead us to the solution of one of the greatest mysteries in physics —the matter-antimatter asymmety problem. Many extensions of SM have been shown to predict a first-order EWPT (e.g. [8–10]), and they can be probed by the future colliders, next generation gravitational wave observatories, dark matter searches, and electron electric dipole moment experiments [11–14].

There also exists some renormalizable models which predict that the electroweak symmetry was never restored or only temporarily restored in the early universe [15–

17]. In all those renormalizable models, it is always the new scalar sectors that are responsible for the electroweak symmetry non-restoration (EWSNR). In this dissertation, I propose a new mechanism for inducing EWSNR by the new fermions in renormalizable models.

In the rest of this chapter, I will explain why it may seem impossible to have fermion-induced EWSNR in any renormalizable models. In chapter 2, I will introduce a mechanism that can overcome those difficulties, and construct several models to illustrate the mechanism. The numerical methods for calculating the finite temperature effective potential and the thermal histories will be described in chapter 3. The physically viable parameter space of these models must satisfy certain theoretical constraints and must not violate any experimental observations, as will be explained in section 4.1. Then, the novel thermal histories of these models and their characteristics will be presented in section 4.2. In chapter 5, I will show how these models can be probed by the future gravitational wave experiments. In the last chapter, I will give a summary and suggest some future research directions.

1.1 Challenges

The conventional quantum field theory is not suitable for calculating observables in the early universe when it was hot and dense. Instead, we can use quantum statistical mechanics to describe the background state of the early universe, and use the conventional quantum field theory for the Hamiltonian of a system that is in thermal equlibrium with the background state. This formalism is known as finite-temperature quantum field theory (FTQFT) ([18] is an excellent introduction). By using FTQFT, we can calculate the one-loop effective potential at finite temperature

$$V_{\text{eff}} = V_0 + \sum_i \left(V_i^{\text{CW}} + V_i^{\text{th}} \right) , \tag{1.1}$$

where V_0 is the tree-level scalar potential, $V_i^{\rm CW}$ is the Coleman-Weinberg potential, and $V_i^{\rm th}$ is the one-loop thermal potential of the $i^{\rm th}$ particle. In the $\overline{\rm MS}$ renormalization scheme, they are given by

$$V_i^{\rm CW} = a_i d_i \frac{m_i^4}{64\pi^2}\left[\log\left(\frac{m_i^2}{\mu^2}\right) - c_i\right], \tag{1.2}$$

$$V_i^{\rm th} = a_i d_i \frac{T^4}{2\pi^2} J_i\left(\frac{m_i^2}{T^2}\right), \tag{1.3}$$

in which $a_i = 1\,(-1)$ for bosons (fermions), $c_i = 3/2\,(1/2)$ for scalars, fermions, and longitudinal components of vector bosons (transverse components of vector bosons), d_i is the number of degrees of freedom, and m_i is the field-dependent tree-level masses of the $i^{\rm th}$ particle. The thermal functions are given by

$$J_i(y^2) = \int_0^\infty dx\, x^2 \log\left[1 - a_i \exp\left(-\sqrt{x^2+y^2}\right)\right]. \tag{1.4}$$

In the high-temperature limit, $m_i^2 \ll T^2$, J_i can be conveniently expanded with respect to y:

$$J_i(y^2) = \begin{cases} -\dfrac{\pi^4}{45} + \dfrac{\pi^2}{12}y^2 + \mathcal{O}(y^3), & i \in \text{bosons} \\ \dfrac{7\pi^4}{360} - \dfrac{\pi^2}{24}y^2 + \mathcal{O}(y^3), & i \in \text{fermions}. \end{cases} \tag{1.5}$$

Thus, at high temperatures, the temperature-dependent part of one-loop effective potential is dominated by the terms that are proportional to T^2

$$V^{\rm th} = \sum_i V_i^{\rm th} \approx \sum_i \frac{\tilde{d}_i m_i^2 T^2}{48}, \tag{1.6}$$

where $\tilde{d}_i = 2d_i\,(d_i)$ for bosons (fermions). By using eq. (1.6), we can determine if the electroweak symmetry was restored in the early universe when the temperatures

were sufficiently high.

For examples, in the SM,

$$\frac{\partial^2 V^{\rm th}}{\partial h^2} \approx T^2 \left(\frac{3}{16} g^2 + \frac{1}{16} g'^2 + \frac{1}{4} y_t^2 + \frac{1}{2} \lambda_h \right) , \tag{1.7}$$

where $g' \, , g \, , y_t \, , \lambda_h$ are gauge coupling for $U(1)_Y \, , SU(2)_L$, top Yukawa coupling, and quartic Higgs self-coupling respectively. Eq. (1.7) implies that the effective potential is a rapidly increasing function of h when T is large. Thus, the effective potential can only be minimized at $h = 0$ and the electroweak symmetry was restored at high temperatures. In some models, electroweak symmetry was always broken at high temperatures. For example, by adding singlet scalar s_i with $O(N_s)$ global symmetry to the SM [15],

$$\begin{aligned} V_0 &= V_{\rm SM,0} + \frac{1}{2} \mu_s^2 (s_i s_i) + \frac{1}{4} \lambda_s (s_i s_i)^2 + \frac{1}{2} \lambda_{hs} h^2 (s_i s_i) \, , \\ \frac{\partial^2 V^{\rm th}}{\partial h^2} \Big|_{h=0} &= T^2 \left(\frac{3}{16} g^2 + \frac{1}{16} g'^2 + \frac{1}{4} y_t^2 + \frac{1}{2} \lambda_h + \frac{N_s}{12} \lambda_{hs} \right) . \end{aligned} \tag{1.8}$$

$\frac{\partial^2 V^{\rm th}}{\partial h^2} \Big|_{h=0} < 0$ when $\lambda_{hs} < 0$ and $|N_s \lambda_{hs}|$ is large enough to overcome the large positive contribution from the SM particles. In that case, the vacuum expectation value (VEV) of h must be nonzero, and therefore the electroweak symmetry is broken. Note that $|\lambda_{hs}|$ must be sufficiently small so that the perturbative unitarity bound is not violated. This is not possible when $N_s = 1$ [11, 19, 20], but possible if N_s is sufficiently large [15]. It is also possible to achieve EWSNR without introducing a large amount of scalars but with more beyond-SM couplings, e.g. the extension of SM Higgs sector that contains two Higgs doublets and a singlet scalar [16].

Now, consider the extension of SM with new fermions (F) of the same species. In the high-temperatures limit, by using eq. (1.6), the contributions of new fermions to

the second derivative of thermal potential is

$$\frac{\partial^2 V_F^{\rm th}}{\partial h^2} = \sum_{i\in F} T^2 \frac{d_F}{48}\frac{\partial^2 m_i^2}{\partial h^2} = T^2 \frac{d_F}{48}\frac{\partial^2}{\partial h^2}\,{\rm Tr}\Big(M_F^\dagger M_F\Big) = T^2 \frac{d_F}{48}\frac{\partial^2}{\partial h^2}\sum_{i,j}|M_{F,ij}|^2\,, \quad (1.9)$$

where M_F is the mass matrix of the new fermions in weak eigenstate basis, and m_i are the mass eigenvalues. In any renormalizable models, each mass matrix element is in the form of $M_{F,ij} = a_0 + a_1 h$, where a_0, a_1 are field-independent complex numbers. Therefore, $\dfrac{\partial^2 V_F^{\rm th}}{\partial h^2} \geq 0$ for all h, which implies EW symmetry is always restored at high temperatures when adding only new fermions in renormalizable models.

However, the analysis above relies on three crucial assumptions. First, eq. (1.6) is valid only when $m_i^2 \ll T^2$. If m_i does not depend on T, then there always exists sufficiently high temperatures such that $m_i \ll T^2$ is satisfied. If m_i increases as T increases for some new fermions, then the analysis above does not hold. In the next chapter, I will propose such a mechanism, and discuss several UV-complete models that realize fermionic-induced EWSNR. Second, the analysis above only consider the thermal effects from the one-loop thermal potential. The traditional perturbative expansion in terms of small coupling constants breaks down at high temperatures due to the infrared divergences generated by the zero Matsubara modes of bosons. Thus, it is necessary to resum the leading part of certain multi-loop diagrams that are known as the daisy diagrams [21–23]. We will consider these higher-order thermal effects in chapter 3. Third, the analysis above assumes $M_{F,ij} = a_0 + a_1 h$, which is generally not true in non-renormalizable models. [24] showed that fermionic-induced EWSNR can be generated by non-renormalizable operators in several effective field theories (EFT), but the electroweak symmetry non-restoration temperature is bounded from above by the EFT cutoff. In this dissertation, I will show that EWSNR can be induced by new fermions even in the renormalizable models. In renormalizable models, we can discuss how the higher-order corrections can impact the stability of the effective

potential and the perturbative unitarity bound in a more transparent way.

Chapter 2

Mechanism and models

In this chapter, I propose a novel mechanism for EWSNR through renormalizable fermionic interactions. I will introduce the mechanism in Section 2.1, write down the scalar potential explicitly in Section 2.2, and discuss the EW symmetry breaking and restoring patterns in the early universe qualitatively in Section 2.3.

2.1 Model definition

Let me start by outlining steps followed in the model building process. In order to achieve fermionic-induced EWSNR, the contributions of new fermions to the one-loop thermal potential must be significant. Thus, the new fermions must couple to the Higgs doublet directly. If the new Yukawa terms contain both the SM fermions and new fermions,it would lead to a sizable mixing between the SM fermions and the new fermions. Such mixing modifies the prediction of the SM fermion coupling, which is heavily constrained experimentally. To form new Yukawa terms without SM fermions, the new models must contain $SU(2)$ fermion doublets and singlets. As discussed in Section 1.1, in order to have $\frac{\partial^2 V_F^{\rm th}}{\partial h^2}\Big|_{h=0} < 0$, we need some new fermions masses with $\frac{\partial^2 m_i^2}{\partial h^2} < 0$. The simplest model that have the aforementioned characteristics is the single-doublet fermion model, which consists of a pair of electroweak doublet

fermions with a vector-like mass term and a electroweak singlet fermion [25,26]. However, this model violates the custodial symmetry, and the new Yukawa couplings are constrained by the experimental bounds on the T parameter [27–29]. In order to allow a larger parameter space for the new Yukawa couplings, the minimal model contains an electroweak doublet fermions and two electroweak singlet Dirac fermions because it posseses an approximate custodial symmetry when the "up-type" Yukawas equal the "down-type" Yukawas (i.e. $y_{NN'i} = y_{EE'i}$ for $i = 1, 2$; see notation conventions below). We will call this model singlet-singlet doublet (SSD) model. The $SU(3)_C \times SU(2)_L \times U(1)_Y$ quantum numbers of new fermions and the new Yukawa terms are

$$\begin{aligned} L^i_{L,R} &= \begin{bmatrix} N^i \\ E^i \end{bmatrix}_{L,R} \sim (1,2)_{-\frac{1}{2}}\,,\ N'^i_{L,R} \sim (1,1)_0\,, E'^i_{L,R} \sim (1,1)_{-1} \\ \mathcal{L}^i_{\text{SSD-yuk}} &= -y^i_{NN'1}\overline{L^i_L}\widetilde{\phi}N'^i_R - y^i_{NN'2}\overline{N'^i_L}\widetilde{\phi}^\dagger L^i_R - y^i_{EE'1}\overline{L^i_L}\phi E'^i_R - y^i_{EE'2}\overline{E'^i_L}\phi^\dagger L^i_R \\ &\quad -m_{Li}(\sigma)\overline{L^i_L}L^i_R - m_{N'i}(\sigma)\overline{N'^i_L}N'^i_R - m_{E'i}(\sigma)\overline{E'^i_L}E'^i_R + h.c.\,, \end{aligned} \tag{2.1}$$

in which ϕ is a $SU(2)_L$ scalar doublet (see Section 2.2). The vector-like masses $m_X(\sigma)$ ($X = N', E', L$) can be generated dynamically, and the mechanism will be discussed in Section 2.3.

We need to introduce more than one generation of SSD fermions to avoid large Yukawa couplings, which violate the perturbative unitarity bound. Furthermore, large Yukawas have substantial effects on the running of Higgs quartic coupling and destabilize the effective potential (will be discussed in Chapter 4). Therefore, we extend the SM with $N_F > 1$ generations of SSD fermions, and the Yukawa Lagrangian reads

$$\mathcal{L}_{\text{yuk}} = \mathcal{L}_{\text{SM-yuk}} + \sum_{i=1}^{N_F} \mathcal{L}^i_{\text{SSD-yuk}} \tag{2.2}$$

Here we assume there is no interaction among different generations, so the generation

indices of the new fermions will be omitted for the rest of dissertation to improve readability.

The (tree-level) physical masses of the new fermions are

$$m_{N1}^2 = \frac{1}{2}\left(A_N^2 - \sqrt{\left(A_N^2\right)^2 - 4\left(\Delta_N^2\right)^2}\right) \tag{2.3}$$

$$m_{N2}^2 = \frac{1}{2}\left(A_N^2 + \sqrt{\left(A_N^2\right)^2 - 4\left(\Delta_N^2\right)^2}\right), \tag{2.4}$$

where

$$A_N^2 = |m_{NN'1}|^2 + |m_{NN'2}|^2 + |m_{N'}|^2 + |m_L|^2, \tag{2.5}$$

$$\Delta_N^2 = |m_L m_{N'} - m_{NN'1} m_{NN'2}|, \tag{2.6}$$

$$m_{NN'j} = \frac{1}{\sqrt{2}} y_{NN'j} h, \qquad (j = 1, 2). \tag{2.7}$$

m_{E1}, m_{E2} have the same expressions, except $N \to E$. The diagonalization of the mass matrix and mixing angles are given in appendix A.

2.2 Tree-level scalar potentials

In this section, I will discuss the scalar sector relevant to this study. In this work, two different scalar sectors will be investigated: the SM extended by SSD (denoted as SM+SSD), and the inert two-Higgs-doublet model (I2HDM) extended by SSD (denoted as I2HDM+SSD). In SM+SSD, ϕ in Eq. (2.1) is the SM Higgs doublet Φ_1. In I2HDM+SSD, the new fermions only couple with the inert Higgs doublet, and ϕ stands for the inert doublet. We will use SM+SSD to give some simple examples in Section 2.3, but the main results in Chapter 4-5 are based on the I2HDM+SSD model. As we will see in the next section, I2HDM+SSD model has a larger parameter space that allow EWSNR, hence more interesting predictions can be derived from

I2HDM+SSD model.

The scalar potential in the Lagrangian of SM is

$$V = -\mu_1^2 \Phi_1^\dagger \Phi_1 + \lambda_1 (\Phi_1^\dagger \Phi_1)^2 \,, \tag{2.8}$$

where $\Phi_1 = \begin{bmatrix} \varphi_1^+ \\ (h_1 + H_1^0 + i\varphi_1^0)/\sqrt{2} \end{bmatrix}$. h_1 is the background field, H_1^0 is the Higgs field, and φ_1^0, $\varphi_1^\pm$ are Goldstone bosons. The effective potential, by definition, only depends on the background field. Its tree-level term is simply

$$V_0(h_1) = -\frac{1}{2}\mu_1^2 h_1^2 + \frac{1}{4}\lambda_1 h_1^4 \,. \tag{2.9}$$

The scalar potential in the Lagrangian of the most general renormalizable two-Higgs-doublet model (2HDM) is

$$\begin{aligned} V = &-\mu_1^2 \Phi_1^\dagger \Phi_1 + \lambda_1 (\Phi_1^\dagger \Phi_1)^2 - \mu_2^2 \Phi_2^\dagger \Phi_2 + \lambda_2 (\Phi_2^\dagger \Phi_2)^2 + \lambda_3 (\Phi_1^\dagger \Phi_1)(\Phi_2^\dagger \Phi_2) + \lambda_4 (\Phi_1^\dagger \Phi_2)(\Phi_2^\dagger \Phi_1) \\ &- \mu_{12}^2 \Phi_1^\dagger \Phi_2 + \frac{\lambda_5}{2}\left(\Phi_1^\dagger \Phi_2\right)^2 + \frac{\lambda_6}{2}\left(\Phi_1^\dagger \Phi_1\right)\left(\Phi_1^\dagger \Phi_2\right) + \frac{\lambda_7}{2}\left(\Phi_2^\dagger \Phi_2\right)\left(\Phi_1^\dagger \Phi_2\right) + \text{h.c.} \,. \end{aligned} \tag{2.10}$$

By requiring $\mathrm{Re}(\mu_{12}^2) = \mathrm{Re}(\lambda_6) = 0$, the second Higgs can have a zero VEV (see Eq. (195) in [30]). We are free to set μ_{12} and λ_k ($k = 3, 4, 5, 6, 7$) at the initial renormalization scale. These couplings remains zero for all scales except λ_3 and λ_4; λ_3 and λ_4 grow slowly as renormalization scale increases, driven by the nonzero EW gauge couplings (see the one-loop RGEs in Chapter 3 and appendix E in [30]). $\mu_{12} = \lambda_l = 0$ ($l = 5, 6, 7$) can also be achieved by imposing a $U(1)$ symmetry on one

of the Higgs doublets. To summarize, we consider the scalar potential of I2HDM

$$V = -\mu_1^2\Phi_1^\dagger\Phi_1+\lambda_1(\Phi_1^\dagger\Phi_1)^2-\mu_2^2\Phi_2^\dagger\Phi_2+\lambda_2(\Phi_2^\dagger\Phi_2)^2+\lambda_3(\Phi_1^\dagger\Phi_1)(\Phi_2^\dagger\Phi_2)+\lambda_4(\Phi_1^\dagger\Phi_2)(\Phi_2^\dagger\Phi_1)\,, \tag{2.11}$$

where $\Phi_j = \begin{bmatrix} \varphi_j^+ \\ (h_j + H_j^0 + i\varphi_j^0)/\sqrt{2} \end{bmatrix}$, $(j = 1, 2)$. Now, h_1 and h_2 are the background fields, and there are five physical Higgs fields H_1^0, H_2^0, φ_2^0, $\varphi_2^\pm$, and three Goldstone bosons φ_1^0, $\varphi_1^\pm$. The tree-level term of the effective potential is

$$V_0(h_1, h_2) = -\frac{1}{2}\mu_1^2 h_1^2 + \frac{1}{4}\lambda_1 h_1^4 - \frac{1}{2}\mu_2^2 h_2^2 + \frac{1}{4}\lambda_2 h_2^4 + \frac{1}{4}(\lambda_3 + \lambda_4)h_1^2 h_2^2\,. \tag{2.12}$$

The tree-level masses of the scalars (as functions of h_1, h_2) are

$$m^2_{H_1^0} = -\mu_1^2 + 3\lambda_1 h_1^2 + \frac{\lambda_3 + \lambda_4}{2}h_2^2\,, \tag{2.13}$$

$$m^2_{\varphi_1^0} = -\mu_1^2 + \lambda_1 h_1^2 + \frac{\lambda_3 + \lambda_4}{2}h_2^2\,, \tag{2.14}$$

$$m^2_{\varphi_1^\pm} = -\mu_1^2 + \lambda_1 h_1^2 + \frac{\lambda_3}{2}h_2^2\,, \tag{2.15}$$

$$m^2_{H_2^0} = -\mu_2^2 + 3\lambda_2 h_2^2 + \frac{\lambda_3 + \lambda_4}{2}h_1^2\,, \tag{2.16}$$

$$m^2_{\varphi_2^0} = -\mu_2^2 + \lambda_2 h_2^2 + \frac{\lambda_3 + \lambda_4}{2}h_1^2\,, \tag{2.17}$$

$$m^2_{\varphi_2^\pm} = -\mu_2^2 + \lambda_2 h_2^2 + \frac{\lambda_3}{2}h_1^2\,. \tag{2.18}$$

At finite temperatures, nonzero $\langle h_2\rangle$ can be induced by thermal loop effects (of the new fermions from SSD model in our case) and the EW VEV becomes $v_h = \sqrt{\langle h_1\rangle^2 + \langle h_2\rangle^2}$. $(\langle h_1\rangle, \langle h_2\rangle)$ is the location of the EW vacuum; it can be either the global minimum (true vacuum) or a local minimum (false vacuum, also known as metastable state) of the effective potential. In general, the EW vacuum state can be metastable if it is not a global minimum of the effective potential, but its lifetime is longer than the age of the universe. In fact, it is very likely that the EW vacuum

predicted by the SM is metastable, but more precise measurements of the top and Higgs masses, and a better knowledge of the Planck scale physics are required to discriminate between whether the EW vacuum in the SM is stable or metastable [31,32].

2.3 Temperature-dependent fermion masses and fermion-induced EWSNR

As mentioned in Section 1.1, one possible solution to induce EWSNR with renormalizable fermion interactions is to have the fermions masses increase as temperature increases. Thus, the mass of new fermions should be generated dynamically. This can be achieved via Yukawa interactions between the new fermions and a real scalar field (denoted by σ) with temperature-dependent VEV. In renormalizable models, such dynamical masses $m_X(\sigma)$ ($X = N', E', L$) can be parameterized as $m_X(\sigma) = m_{X0} + y_X\sigma$. Similar to notations given in Section 2.2, we write $\sigma \equiv s + S$, where s is the VEV of σ field. The m_X terms in the mass eigenvalues formula (Eq. (2.3-2.6)) take the form of

$$m_X(s) = m_{X0} + y_X s\,. \tag{2.19}$$

When $m_L^2 \gg m_{N'}^2,\, m_{E'}^2,\, \dfrac{1}{2}|y_{NN'1}y_{NN'2}|h^2$, the mass eigenvalues are

$$\begin{aligned} m_{N1}^2 &\approx m_{N'}^2 - \frac{m_{N'}\,\mathrm{Re}(y_{NN'1}y_{NN'2})}{m_L}h^2\,, \\ m_{N2}^2 &\approx m_L^2 + \left(\frac{|y_{NN'1}|^2 + |y_{NN'2}|^2}{2} + \frac{m_{N'}\,\mathrm{Re}(y_{NN'1}y_{NN'2})}{m_L}\right)h^2\,, \end{aligned} \tag{2.20}$$

and same for m_{E1}, m_{E2}, except $N \to E$. For simplicity, I will assume all the Yukawa couplings are real and positive. At high temperatures, if the VEV of σ field increases as temperature increases such that $m_L(T) \gg T$, the contributions of the heavier fermions m_{N2} , m_{E2} to the thermal potential are exponentially suppressed (Eq. (1.4)).

Similar to discussion in Section 1.1, at high temperatures,

$$\left.\frac{\partial^2 V^{\rm th}}{\partial h^2}\right|_{h=0} = -a_h T^2 \,. \tag{2.21}$$

In the SM+SSD model, $h = h_1$, a_h is given by

$$\begin{aligned} a_h = & \frac{N_F}{6m_L}\left(m_{N'} y_{NN'1} y_{NN'2} + m_{E'} y_{EE'1} y_{EE'2}\right) \\ & - \left(\frac{3}{16} g^2 + \frac{1}{16} g'^2 + \frac{1}{4} y_t^2 + \frac{1}{2}\lambda_1\right) . \end{aligned} \tag{2.22}$$

If the parameters of the new fermions sector are chosen such that $a_h > 0$, the EW symmetry remains broken at high temperatures. In Eq. (2.22), the largest negative term comes from the top yukawa coupling y_t. In the I2HDM+SSD model, since the new fermions only couple with the inert Higgs doublet (so $h = h_2$) and the inert Higgs doublet does not couple with the top quark, then a_h becomes

$$\begin{aligned} a_h = & \frac{N_F}{6m_L}\left(m_{N'} y_{NN'1} y_{NN'2} + m_{E'} y_{EE'1} y_{EE'2}\right) \\ & - \left(\frac{3}{16} g^2 + \frac{1}{16} g'^2 + \frac{1}{2}\lambda_2\right) . \end{aligned} \tag{2.23}$$

In the I2HDM+SSD model, without the large y_t, $a_h > 0$ can be achieved with smaller N_F, $m_{N'}/m_L$, $y_{NN'i}$, and $y_{EE'i}$. Thus, the I2HDM+SSD model has a larger parameter space for fermion-induced EWSNR.

The functional form of $s(T)$ will affect the evolution of the EW VEV $v_h(T)$. There are many well-motivated models that contain scalar fields with temperature-dependent VEV, for examples, inflaton and quintessence. The form of $s(T)$ depends on the details of the specific models. In this section, we will illustrate the qualitative behavior of the EW symmetry breaking and restoring patterns in a model independent way by parameterizing $s(T)$ as

$$s(T) = \begin{cases} b_0\,, & \text{if } T < T_1 \\ b_0 + b_1(T-T_1)^{n_1} + b_2(T-T_1)^{n_2}\,, & \text{if } T \geq T_1\,, \end{cases} \tag{2.24}$$

without specifying the underlying models, as those details will not affect the one-loop effective potential calculation (assuming σ only couples to the new fermions).

At high temperatures, the spontaneous EW symmetry breaking (EWSB) is induced by new fermions when the heavy fermions (N_2, E_2) are decoupled from the thermal bath because they are too massive compared to the temperature, while the light fermions (N_1, E_1) are light enough compared to the temperature so that their contributions to the thermal potential are significant. Thus, the criteria for finite-temperature fermionic-induced EWSB are

$$m_1(T)/T < c_1\,, \quad m_2(T)/T > c_2\,. \tag{2.25}$$

To simplify the discussion below, we set $m_i \equiv m_{N_i} = m_{E_i}$ (where $i = 1, 2$) and $m_{N'0} = m_{E'0} = 0$. c_1, c_2 are some temperature-independent numbers and c_1, $c_2 \sim \mathcal{O}(1)$ according to the form of thermal potential (Eq. (1.3-1.4)). The exact values of c_1, c_2 depend on the yukawa couplings and the amount of new fermions, but their exact values are not important in the following qualitative discussions (a more quantitative discussion will be given in Section 4.2). This criteria can be rewritten by using Eq. (2.20) at $h = 0$ as

$$c_2/y_L < s(T)/T < c_1/y_{F'}\,, \tag{2.26}$$

where $y_{F'} \equiv y_{N'} = y_{E'}$. Besides Eq. (2.26), N_F is also required to be large enough such that $a_h > 0$. In the following subsections, we will use Eq. (2.26) to explain qualitatively how the temperature dependence of EW VEV $h(T)$ depends on the functional form of $s(T)$. Figure 2.1 gives an example for each case. Those examples are based on the SM+SSD, without considering the higher-order corrections of the

effective potential and various constraints; those issues will be discussed in Chapter 3 and 4. More realistic numerical results will also be given in Chapter 4.

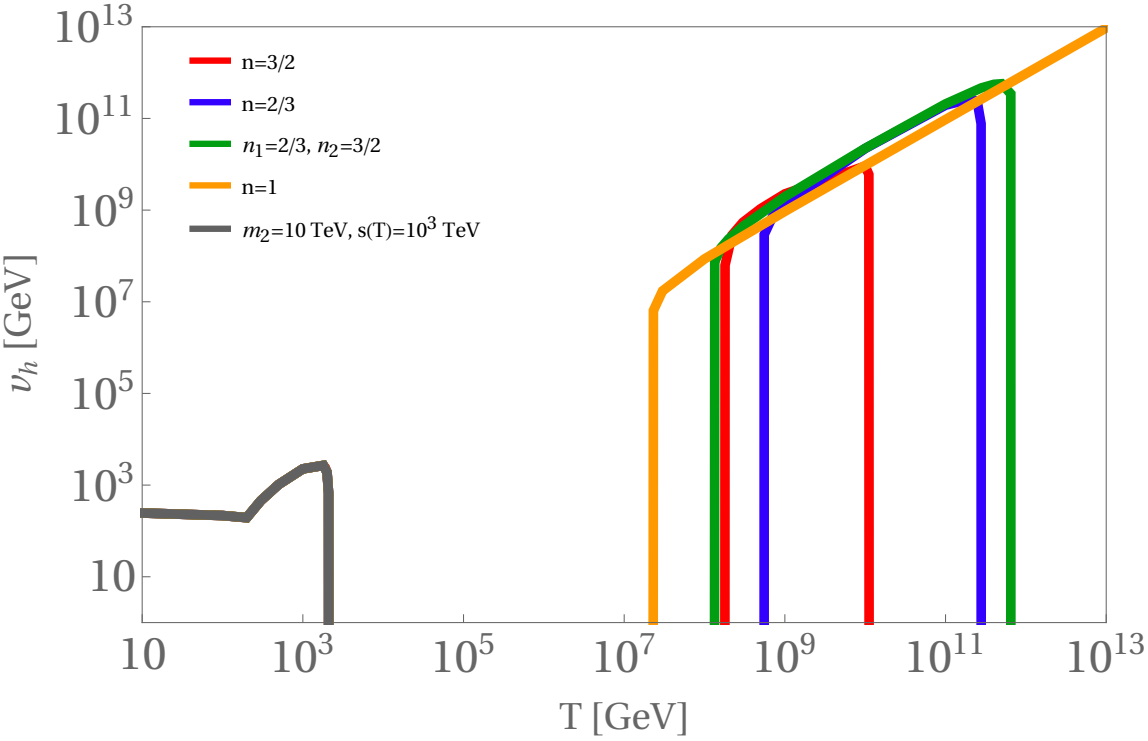

Figure 2.1: The impacts of the functional form of $s(T)$ on the thermal histories.

2.3.1 $s = b_0$

In this case, VEV of σ field is temperature-independent, and it has been studied previously [9,10,24,33]. As expected from Eq. (2.25), the EW symmetry remains broken above the EW scale (in contrast to the SM case, where the cross-over temperature is about 160 GeV) when $T < m_2/c_2$, since only the light fermions contribute siginificantly in the thermal potential. But when temperature is sufficently larger than the masses of the heavy fermions, then the thermal contributions from heavy fermions cancel with those of the light fermions (as explained in Section 1.1), hence we expect

the EW symmetry is restored around

$$T_{cA} \sim \mathcal{O}(m_2/c_2)\,. \tag{2.27}$$

2.3.2 $n_1 = 1$, $b_1 > 0$, $b_2 = 0$

In this case, VEV of σ field increases linearly with temperatures (at high temperatures). Thus, EW symmetry remains broken at all high temperatures as long as b_1 satisfies

$$c_2/y_L < b_1 < c_1/y_{F'}\,. \tag{2.28}$$

Here, high temperatures mean T is large compared to T_1 and b_0/b_1, so that $s(T) \approx b_1 T$. Note that $y_{F'} b_0 = m_1(0)$, thus Eq. (2.28) and $T > b_0/b_1$ imply $T > m_1(0)/c_1$. If $T_1 > T_{cA}$ (T_{cA} as given in Eq. (2.27)), EW symmetry is temporarily restored in intermediate temperatures $T_{cA} < T < T_{cB}$, and becomes broken again when $T > T_{cB}$ (T_{cB} is some temperature larger than T_1 and $m_1(0)/c_1$, but its exact value depends on the parameters of the model). In contrast to the previous case 2.3.1, this case predicts that the EW symmetry is always broken when the temperature is sufficiently high.

2.3.3 $n_1 < 1$, $b_1 > 0$, $b_2 = 0$

In this case, $s(T) \approx b_1 T^{n_1}$ at high temperatures. Thus, according to Eq. (2.26), EW symmetry is broken when

$$T_{cC}^{upper} > T > T_{cC}^{lower}\,. \tag{2.29}$$

where

$$T_{cC}^{upper} \equiv (y_L b_1/c_2)^{1/(1-n_1)}\,, \quad T_{cC}^{lower} \equiv (y_{F'} b_1/c_1)^{1/(1-n_1)}\,. \tag{2.30}$$

Note that the ratio

$$\frac{T_{cC}^{upper}}{T_{cC}^{lower}} = \left(\frac{c_1 y_L}{c_2 y_{F'}}\right)^{1/(1-n_1)} \tag{2.31}$$

is independent of b_1. If $T_{cC}^{lower} > T_{cA}$, EW symmetry is expected to be temporarily restored in intermediate temperatures $T_{cA} < T < T_{cC}^{lower}$. However, unlike Case (2.3.2), EW symmetry is restored above certain temperature T_{cC}^{upper}. Nonetheless, the EW symmetry broken phase can span over a large temperature range in models where n_1 is close to 1, or $y_L/y_{F'}$ is large.

2.3.4 $n_2 > 1$, $b_2 > 0$, $b_1 = 0$

Similar to Case (2.3.3), $s(T)$ is also described by a power law at high temperatures. However, EW symmetry is broken when

$$T_{cD}^{lower} < T < T_{cD}^{upper} \,. \tag{2.32}$$

where

$$T_{cD}^{lower} \equiv (c_2/(y_L b_2))^{1/(n_2-1)} \,, \quad T_{cD}^{upper} \equiv (c_1/(y_{F'} b_2))^{1/(n_2-1)} \,. \tag{2.33}$$

The ratio

$$\frac{T_{cD}^{upper}}{T_{cD}^{lower}} = \left(\frac{c_1 y_L}{c_2 y_{F'}} \right)^{1/(n_2-1)} \tag{2.34}$$

is again independent of b_2. The EW phase structure is very similar to Case (2.3.3).

2.3.5 $n_1 < 1$, $n_2 > 1$, $b_1 > 0$, $b_2 > 0$

In this scenario, $s(T)$ is described by a linear combination of two power laws at high temperatures. EW symmetry is broken when

$$c_2/y_L < b_1 T^{n_1-1} + b_2 T^{n_2-1} < c_1/y_{F'} \,. \tag{2.35}$$

In Case (2.3.3),(2.3.4), we see that the EW broken phases have ratios T^{upper}/T^{lower} that are independent of b_1, b_2. However, in this case, we will see that it is possible to choose b_1, b_2 such that EW is broken in the whole range $T_{cE}^{lower} < T < T_{cE}^{upper}$ for any given pair of $\{T_{cE}^{lower}, T_{cE}^{lower}\}$ (of course, def.(2.24) still restricts $T_1 < T_{cE}^{lower} < T_{cE}^{upper} \leq T_2$).

When $T_l < T < T_u$, $(T_l \equiv T_{cE}^{lower}, T_u \equiv T_{cE}^{upper})$

$$b_1 T_u^{n_1-1} + b_2 T_l^{n_2-1} < s(T)/T < b_1 T_l^{n_1-1} + b_2 T_u^{n_2-1}\,. \tag{2.36}$$

In order to satisfy Eq. (2.35), we can choose b_1, b_2 such that

$$\Delta(T_l, T_u) \begin{bmatrix} b_1 \\ b_2 \end{bmatrix} = \begin{bmatrix} c_1/y_{F'} \\ c_2/y_L \end{bmatrix}\,, \tag{2.37}$$

where

$$\Delta(x_1, x_2) \equiv \begin{bmatrix} x_1^{n_1-1} & x_2^{n_2-1} \\ x_2^{n_1-1} & x_1^{n_2-1} \end{bmatrix}\,. \tag{2.38}$$

The matrix equation (2.37) has a unique solution if $\det\Delta(T_l, T_u) \neq 0$, which requires $n_1 + n_2 \neq 2$. Also, $b_1, b_2 > 0$ implies $n_1 + n_2 > 2$.

Thus, in this case, the EW broken phase can have a temperature range larger than Case (2.3.3),(2.3.4) if b_1, b_2 are chosen properly.

Chapter 3

Beyond the leading order

At finite temperatures, the perturbative expansion of effective potential will break down in certain limits if the thermal loop diagrams with infrared divergences are not resummed properly. In Section 3.1, I will describe a method for resumming a particular set of thermal loop diagrams that are known as the daisy diagrams. In Section 3.2, I will explain the motivation and procedure for calculating the renormalization-group improved effective potential and list the renormalization group equations for our model. In the Section 3.2.1, I will describe the difficulty of computing the renormalization-group improved effective potential in the presence of the multiple mass scales that exist in our model. We address this challenge by adopting the strategy proposed in [34].

3.1 Resummation at finite temperature

At finite temperatures, the boson propogator of n^{th} Matsubara mode is $-i/((2n\pi T)^2+\vec{p}^{\,2}+m_i^2)$ (Eq. (147) in [18]). Thus, we expect infrared divergences appear from the zero Matsubara mode of bosons in the $m_i/T \to 0$ limit (m_i is the tree-level mass of a boson), and the perturbative calculations of the effective potential become unreliable. By power-counting arguments (see section 6 in [18]), we know the multiloop diagrams

with the most dangerous infrared behavior are the so-called daisy diagrams. The $(N+1)$-loop daisy diagram contains N quadratically divergent loops on top of the one-loop self-energy diagram of boson (Figure 3.1). Adding each quadratically divergent loop is equivalent to multiply the diagram by a factor of $\alpha_i \equiv \dfrac{\lambda_i T^2}{m_i^2}$.

Before including the daisy contributions, the one-loop effective potential is

$$V_{\text{eff}}^{\text{1-loop}}(\phi, T) = V_0(\phi) + \sum_i \left(V_i^{\text{CW}}(m_i^2(\phi)) + V_i^{\text{th}}(m_i^2(\phi), T) \right) , \tag{3.1}$$

(here ϕ consists of all the relevant scalar fields). The daisy contributions to all orders can be resummed by replacing the tree-level masses m_i^2 with the Debye masses $\mathcal{M}_i^2 = m_i^2 + \Pi_i$. Similar to the conventional QFT, the thermal self-energies Π_i are calculated by considering the one-loop diagrams of the i^{th} species, but now using the Feynman rules in FTQFT (see Eq. (147) in [18]). In I2HDM+SSD model, Π_i (to the leading

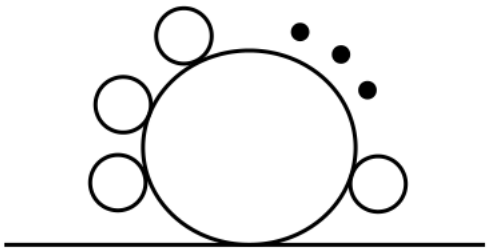

Figure 3.1: An example of daisy diagram for a boson. Assume the mass of the boson is m_i and the coupling corresponds to the each vertex is λ_i.

order in temperature) are

$$\Pi_{h_1} = \Pi_{\varphi_1^0} = \Pi_{\varphi_1^\pm} = \left(\frac{1}{2}\lambda_1 + \frac{1}{6}\lambda_3 + \frac{1}{12}\lambda_4 + \frac{3}{16}g_2^2 + \frac{1}{16}g'^2 + \frac{1}{4}y_t^2\right) T^2$$
$$\Pi_{h_2} = \Pi_{\varphi_2^0} = \Pi_{\varphi_2^\pm} = \left[\frac{1}{2}\lambda_2 + \frac{1}{6}\lambda_3 + \frac{1}{12}\lambda_4 + \frac{3}{16}g_2^2 + \frac{1}{16}g'^2\right.$$
$$\left. + \frac{1}{12}N_F\left(y_{NN'1}^2 + y_{NN'2}^2 + y_{EE'1}^2 + y_{EE'2}^2\right)\right] T^2$$
$$\Pi_{W_L} = \left(2 + \frac{1}{6}N_F\right) g_2^2 T^2$$
$$\Pi_B = \left(2 + \frac{1}{2}N_F\right) g'^2 T^2$$

There is no Π_i for fermions because they do not have zero Matsubara mode and the fermion loops do not suffer from the infrared divergence problem above. On the other hand, the thermal self-energies of transverse components of gauge bosons are suppressed by the gauge symmetry [35]. The Debye masses for the longitudinal components of Z boson and photon are obtained after diagonalizing their squared mass matrix (M_{GB}^2) in the gauge basis. The results are

$$\mathrm{Tr}\, M_{GB}^2 = \frac{1}{4}\left(g_2^2 + g'^2\right)\left(h_1^2 + h_2^2\right) + \Pi_{W_L} + \Pi_B$$
$$\det M_{GB}^2 = \frac{1}{4}\left(g_2^2\Pi_B + g'^2\Pi_{W_L}\right)\left(h_1^2 + h_2^2\right) + \Pi_{W_L}\Pi_B$$
$$\Delta^2 \equiv \left(\mathrm{Tr}\, M_{GB}^2\right)^2 - 4\det M_{GB}^2$$
$$\mathcal{M}_{Z_L}^2 = \frac{1}{2}\left(\mathrm{Tr}\, M_{GB}^2 + \Delta\right)$$
$$\mathcal{M}_{A_L}^2 = \frac{1}{2}\left(\mathrm{Tr}\, M_{GB}^2 - \Delta\right)$$

3.2 Renormalization-group improved potential

Effective potential is directly related to the physical observables (V_{eff} is the generation functional for one-particle irreducible correlation functions of zero external momenta),

hence it is independent of the renormalization scale μ:

$$\frac{dV_{\text{eff}}}{dt} = \left(\mu\frac{\partial}{\partial\mu} + \sum_a \beta_a \frac{\partial}{\partial\lambda_a} - \sum_b \gamma_b\phi_b\frac{\partial}{\partial\phi_b}\right) V_{\text{eff}} = 0\,, \tag{3.2}$$

where $t \equiv \log(\mu/\mu_0)$, and $\lambda_a\,, \phi_b$ are all the couplings and background fields in the model respectively. When V_{eff} satisfies Eq. (3.2), it is "improved" in the sense that the physical observables (e.g. VEV of scalars fields) derived from such V_{eff} are not sensitive to the choice of renormalization scale (μ-dependency of physical observables cannot be eliminated completely because we can only perform perturbation calculations up to certain finite loop order in practice). [34, 36] presented a procedure for constructing renormalization-group improved effective potential that resums all of the leading, next-to-leading,..., and L^{th}-to-leading log terms by using the L-loop effective potential and the renormalization group equations (RGEs) up to $(L+1)$-loop level. In our case, the difficulties lie in that there are multiple mass scales and debye masses depend on multiple scalar fields and temperature. We will improve the one-loop effective potential by using the one-loop RGEs and the procedure in [34, 36] with certain modifications (will be discussed in Section 3.2.1).

The one-loop RGEs for I2HDM+SSD are

$$\begin{aligned}
(4\pi)^2\frac{d\lambda_1}{dt} &= 24\lambda_1^2 - 6y_t^4 + \frac{3}{8}\left[2g_2^4 + \left(g_2^2+g'^2\right)^2\right] + \left(12y_t^2 - 9g_2^2 - 3g'^2\right)\lambda_1 \\
&\quad + 2\lambda_3^2 + 2\lambda_3\lambda_4 + \lambda_4^2 \\
(4\pi)^2\frac{d\lambda_2}{dt} &= 24\lambda_2^2 + \frac{3}{8}\left[2g_2^4 + \left(g_2^2+g'^2\right)^2\right] - \left(9g_2^2 + 3g'^2\right)\lambda_2 + 2\lambda_3^2 + 2\lambda_3\lambda_4 + \lambda_4^2 \\
&\quad + 2N_F\left[2\left(y_{NN'1}^2 + y_{NN'2}^2 + y_{EE'1}^2 + y_{EE'2}^2\right)\lambda_2 - \left(y_{NN'1}^4 + y_{NN'2}^4 + y_{EE'1}^4 + y_{EE'2}^4\right)\right] \\
(4\pi)^2\frac{d\lambda_3}{dt} &= \frac{3}{4}\left[2g_2^4 + \left(g_2^2-g'^2\right)^2\right] + 4\lambda_3^2 + 2\lambda_4^2 + 4(\lambda_3+\lambda_4)(3\lambda_3+\lambda_4) \\
&\quad + \left[-9g_2^2 - 3g'^2 + 6y_t^2 + 2N_F\left(y_{NN'1}^2 + y_{NN'2}^2 + y_{EE'1}^2 + y_{EE'2}^2\right)\right]\lambda_3 \\
(4\pi)^2\frac{d\lambda_4}{dt} &= 3g_2^2g'^2 + 4\lambda_4^2 + 4\lambda_4(\lambda_1+\lambda_2+2\lambda_3)
\end{aligned}$$

$$
\begin{aligned}
&+\left[-9g_2^2-3g'^2+6y_t^2+2N_F\left(y_{NN'1}^2+y_{NN'2}^2+y_{EE'1}^2+y_{EE'2}^2\right)\right]\lambda_4\\
(4\pi)^2\frac{dg'}{dt}&=\left(7+2N_F\right)g'^3\\
(4\pi)^2\frac{dg_2}{dt}&=\left(-3+\frac{2}{3}N_F\right)g_2^3\\
(4\pi)^2\frac{dg_3}{dt}&=-7g_3^3\\
(4\pi)^2\frac{dg_X}{dt}&=-\frac{1}{3}\left(11N_X-8n_F\right)g_X^3\\
(4\pi)^2\frac{dy_t}{dt}&=y_t\left(\frac{9}{2}y_t^2-8g_3^2-\frac{9}{4}g_2^2-\frac{17}{12}g'^2\right)\\
(4\pi)^2\frac{dy_{NN'1}}{dt}&=2y_{N'}y_Ly_{NN'2}+y_{NN'1}\left[\frac{3}{2}y_{NN'1}^2-\frac{3}{2}y_{EE'1}^2+\frac{1}{2}y_{N'}^2+\frac{1}{2}y_L^2\right.\\
&\left.+N_F(y_{NN'1}^2+y_{NN'2}^2+y_{EE'1}^2+y_{EE'2}^2)-\frac{9}{4}g_2^2-\frac{3}{4}g'^2-3\left(N_X-\frac{1}{N_X}\right)g_X^2\right]\\
(4\pi)^2\frac{dy_{EE'1}}{dt}&=2y_{E'}y_Ly_{EE'2}+y_{EE'1}\left[\frac{3}{2}y_{EE'1}^2-\frac{3}{2}y_{NN'1}^2+\frac{1}{2}y_{E'}^2+\frac{1}{2}y_L^2\right.\\
&\left.+N_F(y_{NN'1}^2+y_{NN'2}^2+y_{EE'1}^2+y_{EE'2}^2)-\frac{9}{4}g_2^2-\frac{15}{4}g'^2-3\left(N_X-\frac{1}{N_X}\right)g_X^2\right]\\
(4\pi)^2\frac{dy_{N'}}{dt}&=4y_Ly_{NN'1}y_{NN'2}+y_{N'}\left[3y_{N'}^2+y_{NN'1}^2+y_{NN'2}^2\right.\\
&\left.+2N_F(2y_L^2+y_{N'}^2+y_{E'}^2)-3\left(N_X-\frac{1}{N_X}\right)g_X^2\right]\\
(4\pi)^2\frac{dy_{E'}}{dt}&=4y_Ly_{EE'1}y_{EE'2}+y_{E'}\left[-6g'^2+3y_{E'}^2+y_{EE'1}^2+y_{EE'2}^2\right.\\
&\left.+2N_F(2y_L^2+y_{N'}^2+y_{E'}^2)-3\left(N_X-\frac{1}{N_X}\right)g_X^2\right]\\
(4\pi)^2\frac{dy_L}{dt}&=4\left(y_{N'}y_{NN'1}y_{NN'2}+y_{E'}y_{EE'1}y_{EE'2}\right)+y_L\left[-\frac{3}{2}g'^2+3y_L^2\right.\\
&\left.+\frac{1}{2}\left(y_{NN'1}^2+y_{NN'2}^2+y_{EE'1}^2+y_{EE'2}^2\right)+2N_F(2y_L^2+y_{N'}^2+y_{E'}^2)-3\left(N_X-\frac{1}{N_X}\right)g_X^2\right]\\
(4\pi)^2\frac{d\mu_{h1}^2}{dt}&=\left[12\lambda_1+6y_t^2-\frac{3}{2}(3g_2^2+g'^2)\right]\mu_{h1}^2+(4\lambda_3+2\lambda_4)\mu_{h2}^2\\
(4\pi)^2\frac{d\mu_{h2}^2}{dt}&=\left[12\lambda_2-\frac{3}{2}(3g_2^2+g'^2)+2N_F\left(y_{NN'1}^2+y_{NN'2}^2+y_{EE'1}^2+y_{EE'2}^2\right)\right]\mu_{h2}^2\\
&+(4\lambda_3+2\lambda_4)\mu_{h1}^2\\
(4\pi)^2\frac{d\log h_1}{dt}&=-\left(3y_t^2-\frac{9}{4}g_2^2-\frac{3}{4}g'^2\right)
\end{aligned}
$$

$$(4\pi)^2 \frac{d\log h_2}{dt} = -\left[-\frac{9}{4}g_2^2 - \frac{3}{4}g'^2 + N_F\left(y_{NN'1}^2 + y_{NN'2}^2 + y_{EE'1}^2 + y_{EE'2}^2\right)\right]$$

$\frac{dy_{NN'2}}{dt}$ and $\frac{dy_{EE'2}}{dt}$ are same as the RHS of $\frac{dy_{NN'1}}{dt}$ and $\frac{dy_{EE'1}}{dt}$ respectively, except $1 \leftrightarrow 2$. The one-loop RGEs given above also include the possibility of having n_F generations of N, N', E, E' charged under a new non-abelian gauge $SU(N_X)$ group with a gauge coupling g_X. In those cases, $N_F = N_X\, n_F$. We gain more control on the RG evolution of yukawa couplings of new fermions by introducing new gauge group $SU(N_X)$, but it is not required for having successful fermion-induced EWSNR. Most of the numerical results shown in Chapter 4-5 use $g_X = 0$.

3.2.1 Decoupling scales and $\mu(h_1, h_2, T)$

In order to simplify numerical analysis (without neglecting qualitatively different thermal behaviors), I will make the following choices about the new Yukawa couplings at initial renormalization scale (chosen to be $\mu_0 = 173$ GeV). First, I will choose $y_{NN'1} = y_{NN'2}$ and $y_{N'} = y_{E'}$ at $\mu_0 = 173$ GeV. As can be seen from Eq. (2.23), the contributions to EWSNR stay the same for different choices of individual couplings as long as the combination of $y_{N'}y_{NN'1}y_{NN'2} + y_{E'}y_{EE'1}y_{EE'2}$ stays the same. Second, as mentioned in Chapter 2, $y_{NN'i} = y_{EE'i}$ (at $\mu_0 = 173$GeV) will be required to evade the stringent bound from electroweak precision measurements. The custodial symmetry is explicitly broken due to the nonzero hypercharge gauge coupling g', hence $y_{NN'i}$ and $y_{EE'i}$ (also $y_{N'}$ and $y_{E'}$) are different above the weak scale (it is also evident from the g'^2 terms in their β-functions). Nonetheless, the difference between $y_{NN'i}$ and $y_{EE'i}$ ($y_{N'}$ and $y_{E'}$) stays small in the region where the couplings satisfy the perturbative unitarity bounds. Under those simplifications, the two parameters of interest are $y_{NN'1}$ and $m_{N'}$.

The radiative corrections can generate log terms that explicitly depend on μ.

For example, at one-loop level, $V^{\rm CW}$ contains all the (μ-dependent) log terms (see Eq. (1.2)). In practice, we use perturbation theory to calculate effective potential up to a certain loop order. If μ is not chosen carefully such that there exists large log terms in L-loop $V_{\rm eff}$, then the similar large log terms will also appear at loop orders beyond L, thus such $V_{\rm eff}$ is not a good approximation of the actual effective potential (even if all the couplings satisfy perturbative unitarity bounds). Therefore, a procedure for choosing the correct μ is a critical part in the calculations of RG-improved $V^{\rm CW}$. It is straightforward when a model contains only one mass scale, says $\mathcal{M}$. We will simply choose $\mu = \mathcal{M}$ to remove or minimize the dangerous log terms. However, when there are multiple mass scales $\mathcal{M}_i$ (as in our models), choosing $\mu = \mathcal{M}_1$ does not guarantee $\log\left(\frac{\mathcal{M}^2_{i\neq 1}}{\mu^2}\right)$ are small. We will follow the procedure described in [34] to address this difficulty. In this procedure, the logarithms which contain masses heavier than a given decoupling scale will be absorbed into the couplings via the redefinitions the couplings. And the remaining log terms only depend explicitly on masses that are below the decoupling scale and only these light degrees of freedom contribute to RGEs. Essentially, the solution given by [34] incorporates the decoupling theorem [37,38] and transforms a problem of finding μ in the presence of multiple mass scales into a problem of identifying the appropriate decoupling scales that separate the parameter space of background fields into several regions such that each region contains only a single relevant mass scale. Therefore, there is an unambiguous choice of μ in each region, and such μ is necessarily a function of the background fields.

In our cases, the relevant mass scales are the debye masses of all particles in the model (see Section 3.1). From Eq. (2.20), we can see that $m_{N'}$ and m_L ($m_{E'} \approx m_{N'}$ as explained above) are the suitable decoupling scales. They separate the h_2-field's direction into three regions:

$$
\begin{aligned}
A: &\quad m_L < y_{NN'1} h_2 \\
B: &\quad m_{N'} < y_{NN'1} h_2 < m_L \\
C: &\quad y_{NN'1} h_2 < m_{N'}
\end{aligned}
$$

In region A, all new fermions are considered to be light degrees of freedom. The RGEs are same as above. In region B, only m_L is the heavy scale, hence only N and E fields are decoupled. The RGEs given above are modified by removing all the terms originated from the Feynman diagrams involving the N and E fields (note N and E are flavor eigenstates as defined in Section 2.1). In region C, $m_{N'}$ and m_L are the heavy scales. All the new fermions fields N', E', N, E are decoupled. The RGEs are modified by removing all the terms originated from the Feynman diagrams involving the new fermions.

In region B, the renormalization scale choice and one-loop RGEs are (only shows the couplings and fields that required modifications with respect to region A):

$$
\mu^2 = \max\{\mathcal{M}_i^2(h_1, h_2, T),\ (173\,\mathrm{GeV})^2\}_{i \notin \{N_2, E_2\}} \tag{3.3}
$$

$$
\begin{aligned}
(4\pi)^2 \frac{d\lambda_2}{dt} &= 24\lambda_2^2 + \frac{3}{8}\left[2g_2^4 + \left(g_2^2 + g'^2\right)^2\right] - \left(9g_2^2 + 3g'^2\right)\lambda_2 + 2\lambda_3^2 + 2\lambda_3\lambda_4 + \lambda_4^2 \\
(4\pi)^2 \frac{d\lambda_3}{dt} &= \frac{3}{4}\left[2g_2^4 + \left(g_2^2 - g'^2\right)^2\right] + 4\lambda_3^2 + 2\lambda_4^2 + 4(\lambda_3 + \lambda_4)(3\lambda_3 + \lambda_4) \\
&\quad + \left(-9g_2^2 - 3g'^2 + 6y_t^2\right)\lambda_3 \\
(4\pi)^2 \frac{d\lambda_4}{dt} &= 3g_2^2 g'^2 + 4\lambda_4^2 + 4\lambda_4(\lambda_1 + \lambda_2 + 2\lambda_3) \\
&\quad + \left(-9g_2^2 - 3g'^2 + 6y_t^2\right)\lambda_4 \\
(4\pi)^2 \frac{dg'}{dt} &= \left(7 + \frac{4}{3}N_F\right) g'^3 \\
(4\pi)^2 \frac{dg_2}{dt} &= -3g_2^3
\end{aligned}
$$

$$
\begin{aligned}
(4\pi)^2\frac{dg_X}{dt} &= -\frac{1}{3}\left(11N_X - 4n_F\right)g_X^3 \\
\frac{dy_{NN'i}}{dt} &= \frac{dy_{EE'i}}{dt} = \frac{dy_L}{dt} = 0 \\
(4\pi)^2\frac{dy_{N'}}{dt} &= y_{N'}\left[3y_{N'}^2 + 2N_F(y_{N'}^2 + y_{E'}^2) - 3\left(N_X - \frac{1}{N_X}\right)g_X^2\right] \\
(4\pi)^2\frac{dy_{E'}}{dt} &= y_{E'}\left[-6g'^2 + 3y_{E'}^2 + 2N_F(y_{N'}^2 + y_{E'}^2) - 3\left(N_X - \frac{1}{N_X}\right)g_X^2\right] \\
(4\pi)^2\frac{d\mu_{h2}^2}{dt} &= \left[12\lambda_2 - \frac{3}{2}(3g_2^2 + g'^2)\right]\mu_{h2}^2 + (4\lambda_3 + 2\lambda_4)\mu_{h1}^2 \\
(4\pi)^2\frac{d\log h_2}{dt} &= -\left(-\frac{9}{4}g_2^2 - \frac{3}{4}g'^2\right)
\end{aligned}
$$

In region C, the renormalization scale choice and the one-loop RGEs are (only shows the couplings and fields that required modifications with respect to region B):

$$
\mu^2 = \max\{\mathcal{M}_i^2(h_1, h_2, T),\ (173\,\mathrm{GeV})^2\}_{i\notin\{N_1, E_1, N_2, E_2\}} \tag{3.4}
$$

$$
\begin{aligned}
(4\pi)^2\frac{dg'}{dt} &= 7g'^3 \\
(4\pi)^2\frac{dg_X}{dt} &= -\frac{11}{3}N_X g_X^3 \\
\frac{dy_{N'}}{dt} &= \frac{dy_{E'}}{dt} = 0
\end{aligned}
$$

Since the couplings and fields depend on μ, Eq. (3.3-3.4) define μ as an implicit function of h_1, h_2, and T. In order to reduce computational time, we will use a multi-steps method to approximate $\mu(h_1, h_2, T)$ instead of solving those implicit equations for every (h_1, h_2, T). In region C, we will use $\mu = 173\,\mathrm{GeV}$ for the RHS of Eq. (3.4) to get the first approximate renormalization scale μ_1. Then, use $\mu = \mu_1$ for the RHS of Eq. (3.4) to get the second μ_2. The previous step is repeated until the error falls within the desired tolerance. The couplings and fields run as functions of $t = \log(\mu/\mu_0)$ according to the RGEs. $\{\mu_n\}$ is divergent only when the masses

in RHS of Eq. (3.4) increases (or decreases) at a rate faster than $\mu = \mu_0 e^t$, which implies the couplings or fields changes more rapidly than e^t and signals a breakdown of the perturbative theory. We use the same multi-steps procedure to estimate μ in region B and A, except in the first step, $\mu = m_{N'}$ and $\mu = m_L$ are used respectively. In our numerical studies, we found that two-steps approximations of $\mu(h_1, h_2, T)$ are sufficient because errors ϵ in μ is $\log \epsilon$ in t.

Chapter 4

Thermal histories and constraints

This chapter has two main objectives. The first goal is to discuss theoretical and the experimental constrains on the parameter space of I2HDM+SSD model that allows fermion-induced EWSNR. The second goal is to study the characteristics of the thermal histories (i.e the $v - T$ graphs) within the allowed parameter space. The main focus will be on elucidating how the model parameters affect the thermal histories. All the numerical results presented in this chapter are based on I2HDM+SSD model and the RG-improved effective potential that is described in Chapter 3. In Section 4.2.1, we consider a more general I2HDM+SSD model, and provide benchmarks with large v_h/T. These benchmarks predict gravitational wave signals that can potentially be detected by future gravitational wave observatories.

4.1 Theoretical and experimental constraints

4.1.1 Collider constraints

At $T = 0$ and $\mu = m_t$, we have $\langle h_2 \rangle = 0$ and $\lambda_3 = \lambda_4 = 0$, hence $m_{H_2^0} = m_{\varphi_2^0} = m_{\varphi_2^\pm}$ by Eq. (2.16-2.18). The width of Z boson was measured very precisely at Large Electron–Positron Collider (LEP), which implies $m_Z < m_{H_2^0} + m_{\varphi_2^0}$, $2m_{\varphi_2^\pm}$ [39, 40].

Thus,

$$m_{H_2^0},\, m_{\varphi_2^0},\, m_{\varphi_2^\pm} > m_Z/2\,. \tag{4.1}$$

In our numerical studies, the inert scalars are required to be heavier than 46 GeV at $T = 0$, $\mu = 173\,\text{GeV}$.

LEP experiments also set lower mass limits for charged vector-like heavy leptons (F) [41]:

$$m_F \geq 102.1\,\text{GeV} \qquad (\text{with } F^\pm \to F^0 W^\pm \text{ decay mode})\,, \tag{4.2}$$

$$m_F \geq 102.6\,\text{GeV} \qquad (\text{stable})\,. \tag{4.3}$$

In our numerical studies, all new fermions are required to be heavier than 103 GeV.

4.1.2 Perturbative unitarity bounds

The conservation of probability implies that S-matrix is unitary. A direct consequence of this simple fact is the optical theorem, which can be used to derive a bound on the J-partial wave amplitude of elastic scattering in high-energy limit (see sec.24.1.5 in [42]): $|a_J|^2 \leq |\,\text{Im}\, a_J|$. Thus,

$$|a_J| \leq 1\,, \quad |\,\text{Re}\, a_J| \leq \frac{1}{2}\,. \tag{4.4}$$

Our effective potential is accurate only when the couplings in our model are sufficiently small such that the perturbative theory is valid. Thus, it is necessary to know when the couplings are too large, and Eq. (4.4) provides a simple yet poweful way to determine the upper bounds on the magnitude of couplings (known as the perturbative unitarity bounds). Since the main concern here is the validity of the perturbative expansion of S-matrix, it is sufficient to impose condition (4.4) on the $J = 0$ partial

wave for tree-level scattering amplitudes of relevant processes [19]:

$$a_0 = \frac{1}{32\pi}\int_{-1}^{1} d(\cos\theta)\mathcal{M}\,, \quad |\operatorname{Re} a_J| \leq \frac{1}{2} \tag{4.5}$$

Eq. (4.5) implies that the eigenvalues (denoted as e_i) of $J = 0$ (or S-wave) amplitudes of tree-level scalar-scalar, (longitudinal components of) weak gauge boson-gauge boson, and scalar-gauge boson scatterings satisfy

$$|e_i| \leq 8\pi\,. \tag{4.6}$$

The analytical expressions of e_i are usually complicated for a general 2HDM [43], but they are much simpler in our case [44]:

$$\begin{aligned} &e_{1,2} = \lambda_3 \pm \lambda_4, \quad e_{3,4} = \lambda_3, \quad e_{5,6} = \lambda_3 + 2\lambda_4, \quad e_{7,8} = -(\lambda_1+\lambda_2) \pm \sqrt{(\lambda_1-\lambda_2)^2+\lambda_4^2}, \\ &e_{9,10} = -3(\lambda_1+\lambda_2) \pm \sqrt{9(\lambda_1-\lambda_2)^2+(2\lambda_3+\lambda_4)^2}, \quad e_{11,12} = -(\lambda_1+\lambda_2) \pm |\lambda_1-\lambda_2|. \end{aligned} \tag{4.7}$$

As pointed out in [44], the set of equations above imply

$$\lambda_2 \leq \frac{4\pi}{3}, \quad \lambda_3 + \lambda_4 \lesssim 4\pi - \frac{3\lambda_1}{2}\,. \tag{4.8}$$

Similarly, by imposing Eq. (4.5) on fermion-fermion scattering mediated by scalars (in the high-energy limit), we can obtain the upper bounds on yukawa couplings of new fermions [10, 45]:

$$|y_{NN'i}|, |y_{EE'i}|, |y_L| \leq \sqrt{4\pi}\,, \quad (i = 1, 2)\,. \tag{4.9}$$

$|y_{N'}|$ and $|y_{E'}|$ are always smaller than $|y_L|$ in our cases (see Section 2.3).

4.1.3 Vacuum stability

A vacuum state is stable if it is the global minimum of V_{eff}. It is also possible to have a vacuum state at the local minimum of V_{eff}. As will be explained in Section 5.1, such state can decay to the global minimum (or other deeper local minima) of V_{eff} and its decay rate can be calculated. If the decay rate is sufficiently small, then the transition to the global minimum will never complete and the vacuum state will stay at the local minimum; such vacuum state is known as metastable state. For example, $V_{\text{eff}}(h)$ of the SM has a global minimum at extremely large field $\langle h\rangle_{\text{global}} > M_P$ ($M_P = 1.22 \times 10^{19}\,\text{GeV}$ is the Planck scale) [46], but the physical EW vacuum that we observe today ($\langle h\rangle_{\text{exp}} = 246\,\text{GeV}$) is a local minimum of $V_{\text{eff}}(h)$ of the SM. In the SM, the probability that $\langle h\rangle_{\text{exp}}$ has decayed in the past history of the universe is estimated to be $\lesssim 10^{-500}$ (see Fig. 7 in [31]), thus $\langle h\rangle_{\text{exp}}$ is metastable.

In I2HDM+SSD, it is sufficient to analyze the quartic terms $\frac{1}{4}\lambda_1 h_1^4 + \frac{1}{4}\lambda_2 h_2^4 + \frac{1}{4}(\lambda_3+\lambda_4)h_1^2 h_2^2$ when determining if V_{eff} has a global minimum at a given temperature. λ_3, λ_4 are always positive (they are set to be zero for $\mu(h_1, h_2) \leq 173\,\text{GeV}$ and increase slowly for $\mu(h_1, h_2) > 173\,\text{GeV}$), so they will not destabilize V_{eff}. Similar to the SM case, $\beta(\lambda_1)$ is dominated by the negative term from top yukawa coupling, hence λ_1 is driven to small negative value for large $\mu(h_1, h_2)$. Nonetheless, also similar to the SM case, the decay rate to deeper minimum located at very large h_1 is negligible. Thus, the only concern here is the RG evolution of λ_2. We need sufficiently large $N_F y_{NN'1}^2$ in order to have fermion-induced EWSNR. To avoid large negative contributions from the N_F term in $\beta(\lambda_2)$ in region A (see Section 3.2), λ_2 and $y_{NN'1}$ are required to satisfy

$$\lambda_2 \gtrsim y_{NN'1}^2/2\,. \tag{4.10}$$

Note that λ_2 can be smaller than $y_{NN'1}^2/2$ at initial renormalization scale and still satisfy condition (4.10) in region A (see Figure 4.6 (right panel)). For our bench-

marks, we numerically checked if $\lambda_2(T, h_1, h_2) \gtrsim 0$ for whole region (h_1, h_2) where the perturbative unitary bounds are satisfied. V_{eff} can have metastable vacuum state if λ_2 has small negative value in intermediate region, provided that the transition rate to the global minimum is sufficiently small (see Section 5.3).

4.1.4 Thermal equilibrium conditions

The central assumption of FTQFT is all the particle species of interest are in thermal equilibrium. This requires the interactions rate among those particles to be faster than the expansion rate of the universe. A simple rule of thumb for maintaining thermal equilibrium between particle species i and j is

$$\Gamma_{ij} \gtrsim H\,, \tag{4.11}$$

where H is Hubble rate and $\Gamma_{ij} = n_i \langle \sigma_{ij} v_{\text{rel}} \rangle$ is the interaction rate per particle between species i (with number density n_i) and j [47]. $\langle \sigma_{ij} v_{\text{rel}} \rangle$ is the thermal average of the product of cross section and relative velocity of between initial particles (see appendix B). In radiation-dominated epoch, H grows as T^2/M_P (M_P is the Planck scale), but generally Γ_{ij} grows as T or slower, as we shall see below. Thus, we expect the system of interest was out of equilibrium when T is sufficiently high. In the following paragraphs, I will use the thermal equilibrium condition (4.11) to estimate the temperature upper limit for the broken EW phase induced by the new fermions in I2HDM+SSD model.

The EWSNR mechanism introduced in Chapter 2 requires the weak gauge bosons, Φ_2, N_1, E_1, and σ to be in thermal equilibrium. When $T \gg m_Z$, the interactions mediated by weak gauge bosons have [47]

$$\langle \sigma_{ij} v_{\text{rel}} \rangle \sim \frac{\alpha_W^2}{T^2}\,. \tag{4.12}$$

If the target species i is relativistic, then

$$n_i \approx c_i T^3\,, \quad c_i \equiv \frac{\zeta(3)}{\pi^2} d_i \left(\frac{3\zeta(3)}{4\pi^2} d_i\right) \text{ for bosons (fermions)} \tag{4.13}$$

In radiation-dominated epoch,

$$H \approx c_H\, d_{\text{eff}}^{1/2}\, \frac{T^2}{M_P}\,, \quad c_H \equiv \left(\frac{8\pi^3}{90}\right)^{1/2} \tag{4.14}$$

where

$$d_{\text{eff}} = \sum_{b \in \text{rel. bosons}} d_b + \frac{7}{8} \sum_{f \in \text{rel. fermions}} d_f \tag{4.15}$$

is the effective degrees of freedom of relativitic species that are in thermal equilibrium and d_i are defined in Chapter 1. The 7/8 factor in d_{eff} accounts for the difference in Bose-Einstein and Fermi-Dirac statistics [47]. Thus, Eq. (4.11) implies the species with interactions mediated by weak gauge bosons are in thermal equilibrium when

$$T \lesssim 10^{14}\,\text{GeV} \left(\frac{10^3}{d_{\text{eff}}}\right)^{1/2}\,. \tag{4.16}$$

In I2HDM+SSD model, $d_{\text{eff}} \approx 106.75 + 7N_F$. Therefore, the weak gauge bosons and Φ_2 are in thermal equilibrium for temperatures well above the weak scale when $N_F \sim \mathcal{O}(100)$. The same dimensional analysis argument is applicable for interactions mediated by photons, except $\alpha_w \to \alpha$, thus

$$T \lesssim 10^{13}\,\text{GeV} \left(\frac{10^3}{d_{\text{eff}}}\right)^{1/2}\,. \tag{4.17}$$

Hence, all the charged particles, including E_1, are also in thermal equilibrium for a large range of temperatures and N_F.

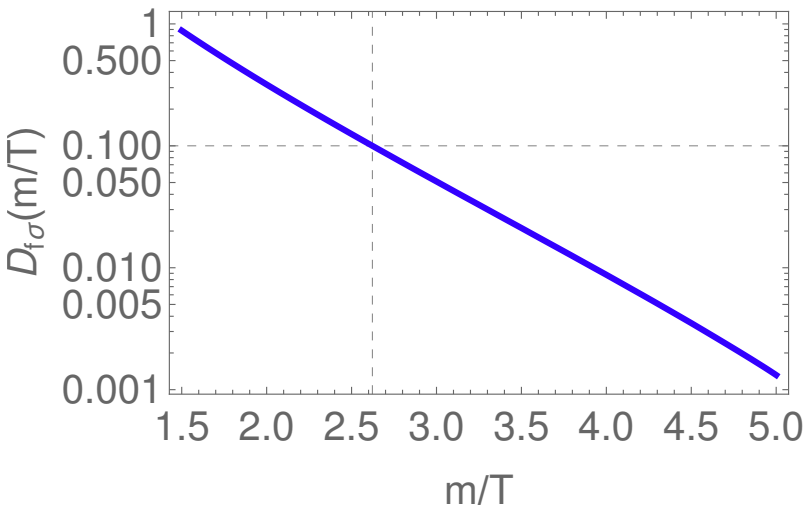

Figure 4.1: $D_{f\sigma}(m/T)$ decreases rapidly as the mass-to-temperature ratio m/T of the mediator increases. $D_{f\sigma} > 0.1$ for $m/T < 2.6$, but $D_{f\sigma} < 1.5 \times 10^{-3}$ for $m/T \geq 5$.

Applying similar argument to $\Gamma(f_i f_i \to \sigma\sigma)$ ($f \in \{N, E\}$, $i \in \{1, 2\}$) gives

$$T \lesssim 10^{13}\,\text{GeV} \left(\frac{10^3}{d_{\text{eff}}}\right)^{1/2} \left(\frac{y_{f_i f_i \sigma}^2/(4\pi)}{\alpha}\right)^2 \equiv T_{U0}^{\text{eq}} \quad (m_{fi} \ll T)\,, \tag{4.18}$$

where $y_{f_i f_i \sigma}$ are given in Appendix A. However, the argument above does not take into account the mass of the fermion mediator. When fermion-induced EWSNR occurs, m_{f2}/T are larger than 1. Also, fermion-induced EWSNR is harder to achieve with small m_{f1}/T, as a_h depends on $m_{f'}/m_f \approx m_{f1}/m_{f2}$ (see Eq. (2.23)). Thus, we calculate $\langle \sigma_{ij} v_{\text{rel}} \rangle$ without assuming $m_{fi} \ll T$ and get

$$T \lesssim T_{U0}^{\text{eq}}\, D_{f\sigma}(m_{fi}/T)\,, \tag{4.19}$$

where T_{U0}^{eq} is the temperature upper limit given in Eq. (4.18) when the fermion mediators are assumed to be massless. The expression of $D_{f\sigma}$ and $\Gamma(f_i f_i \to \sigma\sigma)$ are given in Appendix B. As shown in Figure 4.1, the temperature upper limit is significantly suppressed by $D_{f\sigma}$ as m_{fi}/T increases. Nonetheless, when the light fermions have $m_{f1}/T < 2.6$ (see Figure 4.1), the temperature upper limit is still close to the massless

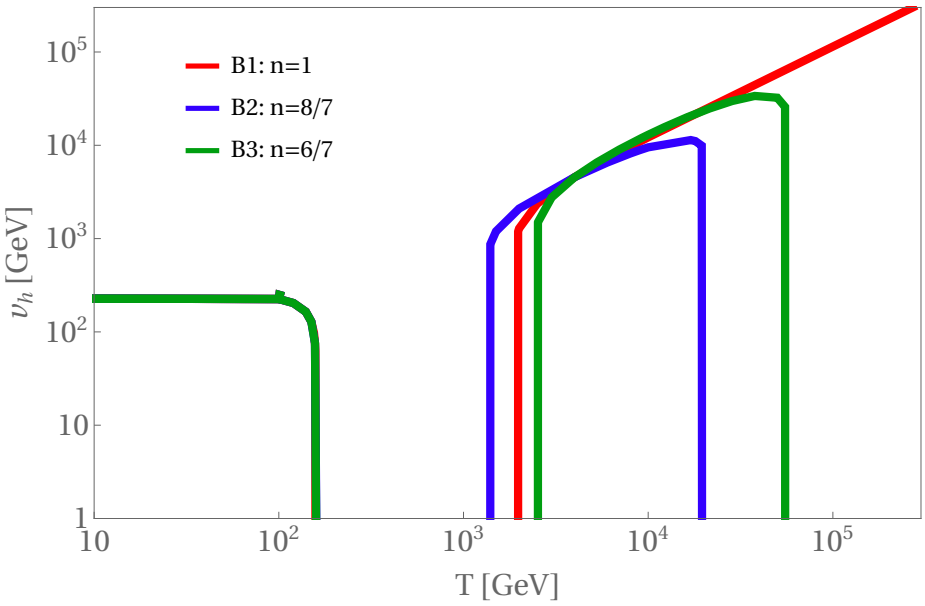

Figure 4.2: Thermal histories for different functional forms of $s(T)$. Details of benchmark B1 are given in Table 4.1. Model parameters for B2 and B3 are same as B1, except $n = 8/7$ and $n = 6/7$ respectively.

limit $T_{U0}^{\rm eq}$. For example, for $y_{f_1 f_1 \sigma} \approx y_{N'} = 0.05$, $N_F \sim 100$, and $m_{f1}/T \approx 1.8$, the system of interest is in thermal equilibrium up to $T_{U0}^{\rm eq} D_{f\sigma}(1.8) \sim 10^9\,{\rm GeV}$, which is still well above the weak scale. An interesting scenario is a FOPT occurs even if $s(T)$ is linear, around temperature $T = T_{U0}^{\rm eq}\, D_{f\sigma}$ that is much higher than the weak scale.

4.2 Characteristics of thermal histories

In this section, I will discuss the characteristics of thermal histories for $s(T)$ in form of $b_0 + b_1 T^n$ (see Eq. (2.24)) by examining several benchmarks within the parameter space that satisfy the constraints in previous section. All results are computed by using the RG-improved $V_{\rm eff}$ described in Chapter 3.

First, we compare benchmarks B1, B2, and B3, which differ in n only. The model parameters of B1 are given in Table 4.1. Comparing Figure 4.2 with Figure 2.1, we can see that the qualitative features of the thermal histories do not change after higher-order corrections are included: when $s(T)$ are nonlinear, EW symmetry is broken

Table 4.1: Input parameters and couplings at initial renormalization scale $\mu_0 = 173$ GeV for benchmark B1. Also, $y_{N'i} = y_{E'i}$, $y_{NN'1i} = y_{NN'2i} = y_{EE'1i} = y_{EE'2i}$, $c_L \equiv b_1 y_L T_L^{n-1}$, where $T_L = 4$ TeV.

N_F	$y_{N'i}$	y_{Li}	$y_{NN'1i}$	n	c_L	$y_{Li}b_0$	T_1	λ_{2i}	$-\mu_{2i}^2$
50	0.05	0.1	0.15	1	4	2 TeV	10 GeV	0.012	$(100\,\text{GeV})^2$

when the fermion-induced EWSNR mechanism described in Chapter 2 is activated for a finite range of temperatures; when $s(T)$ is linear, EW symmetry stays broken once fermion-induced EWSNR mechanism is turned on and $T \lesssim T_{U0}^{\text{eq}}\, D_{f\sigma}(m_{f1}/T)$ as required by the thermal equlibrium constraint. When $T \lesssim 160$ GeV, the thermal histories of B1-B3 are basically same as the SM case because the thermal effects of new fermions are very small when T is small compared to the masses of new fermions ($m_{N1} \approx 1$ TeV and $m_{N2} \approx 2$ TeV at $T = 0$ in B1-B3). Although this is different from Figure 2.1, it is due to the different choices of m_{N1} and m_{N2} at $T = 0$ and unrelated to the higher-order corrections (benchmarks in Figure 2.1 use $m_{N1} \approx 500$ GeV and $m_{N2} \approx 10$ TeV at $T = 0$). Figure 4.3 helps to illustrate when the fermion-induced EWSNR mechanism is activated. For example, in B3, the EW symmetry is broken when $m_{N'}/T < 2.5$ and $m_L/T > 2.8$; i.e. $c_1 = 2.5$, $c_2 = 2.8$ using notations of Section 2.3. B3 and B8 only differ in $y_{N'}$ and y_L and have the same $y_{N'}/y_L$, so we expect B8 has about same c_1, c_2. Indeed, in Figure 4.3 (upper left panel), the horizontal green and red line intersect with the $m_{N'}/T$ and m_L/T dashed curves almost exactly at $T = 9.5 \times 10^4$ GeV and $T = 6.7 \times 10^6$ GeV respectively, which are the lower and upper temperature limit of the EW broken phase for B8 (see lower panel of Figure 4.3). This also explains why the lower and upper temperature limit of the EW broken phase shift to higher values and the duration of EW broken phase is longer when $y_{N'}$ and y_L increase ($y_{N'}/y_L$ is kept fixed) if $n < 1$. If $n > 1$, reducing $y_{N'}$ and y_L affects not only the lower, upper temperature limit, and duration of the EW broken phase, but may also create two separate EW broken phases, as in B9

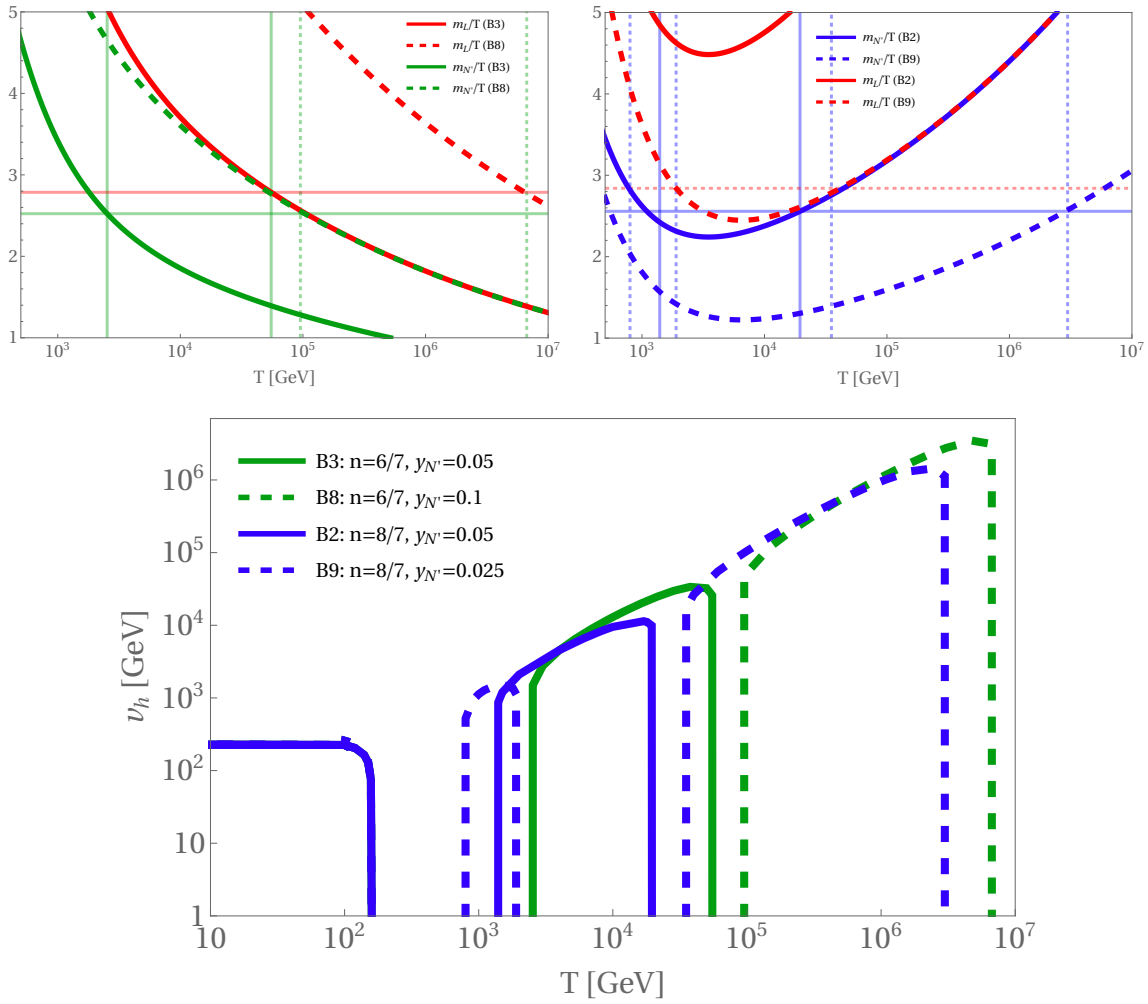

Figure 4.3: **Upper Left**: $n = 6/7$. The solid vertical lines indicate the lower and upper temperature limits of EW broken phase in B3 and the dashed vertical lines indicate the lower and upper temperature limits of EW broken phase in B8 (see **Lower** panel). The fermion-induced EWSNR mechanism is activated when $m_{N'}/T$ is below the green horizontal line and m_L/T is above the red horizontal line. **Upper Right**: $n = 8/7$. The solid vertical lines indicate the lower and upper temperature limits of EW broken phase in B2 and the dashed vertical lines indicate the lower and upper temperature limits of the two EW broken phases in B9 (see **Lower** panel). The fermion-induced EWSNR mechanism is activated when $m_{N'}/T$ is below the blue horizontal line and m_L/T is above the red (dashed) horizontal line. **Lower**: Thermal histories of B2, B3, B8, B9. All benchmarks have $y_{N'}/y_L = 0.5$, $b_1 = (4/0.1)(4\,\text{TeV})^{1-n}$, $b_0 = 1\,\text{TeV}/y_{N'}$.

(see lower panel of Figure 4.3). This again can be explained by analyzing the $m_{N'}/T$ and m_L/T curves. When T is low, $s(T)$ is dominated by b_0, so $s(T)/T$ must be a

decreasing function of T regardless of n. However, when T is high, $s(T)/T$ is an increasing function of T if $n > 1$, hence $m_{N'}/T$ and m_L/T curves have minima. If the minimum of m_L/T curve drops below c_2 after decreasing y_L, then two EW broken phases appear; they are separated by a EW symmetry phase in which $m_L/T < c_2$. As shown in Figure 4.3 (upper right panel) , the red dashed horizontal line ($c_2 = 2.84$) intersects with m_L/T (red dashed) curves of B9 almost perfectly at $T = 1.9 \times 10^3$ GeV and $T = 3.5 \times 10^4$ GeV (blue dashed vertical lines), which are the upper temperature limit of the first EW broken phase and the lower temperature limit of the second EW broken phase respectively.

We can use the similar arguments to explain how b_1 affects the thermal histories. Before discussing the effects of b_1, it is useful to introduce two auxilliary parameters, c_L and T_L, defined by $c_L \equiv b_1 y_L T_L^{n-1}$; c_L is dimensionless and T_L has the dimension of temperature. The physical meaning of b_1 is less transparent when comparing benchmarks with different n since the mass dimension of b_1 depends on n, while c_L and T_L have the same physical interpretations for different n. It is useful to choose $c_L T_L$ such that $(y_L b_0/(c_L T_L))^{1/n} \ll 1$, so that $c_L \approx m_L(T_L)/T_L$. If $n < 1$ ($n > 1$), T_L is approximately the upper temperature limit of EW broken phase when $c_L = c_2$ ($(y_{N'}/y_L)c_L = c_1$), as shown by the solid curves (i.e. benchmarks B2, B3) in the upper panel of Figure 4.3. Usually we do not know the exact values of c_1 and c_2 when setting the input parameters, but it is not difficult to pick c_L that satisfy $c_2 \lesssim c_L \lesssim (y_{N'}/y_L)c_1$, so that the chosen T_L lies within the temperature range of EW broken phase. Thus, we can control roughly when the EW symmetry is broken by using T_L and c_L. For examples, B1-B3 share the same $c_L = 4$ and $T_L = 4$ TeV, so their $v_h(T)$ curves intersect around $T = T_L$, as shown in Figure 4.2. b_1 of B1-B3 are 40, $12.2\,\mathrm{GeV}^{-1/7}$, $131\,\mathrm{GeV}^{1/7}$ respectively and it is not useful to compare these numbers directly. In Figure 4.4 (left panel), we investigate the effects of b_1 by changing the dimensionless parameter c_L. Reducing c_L causes the $m_{N'}/T$ and m_L/T curves to

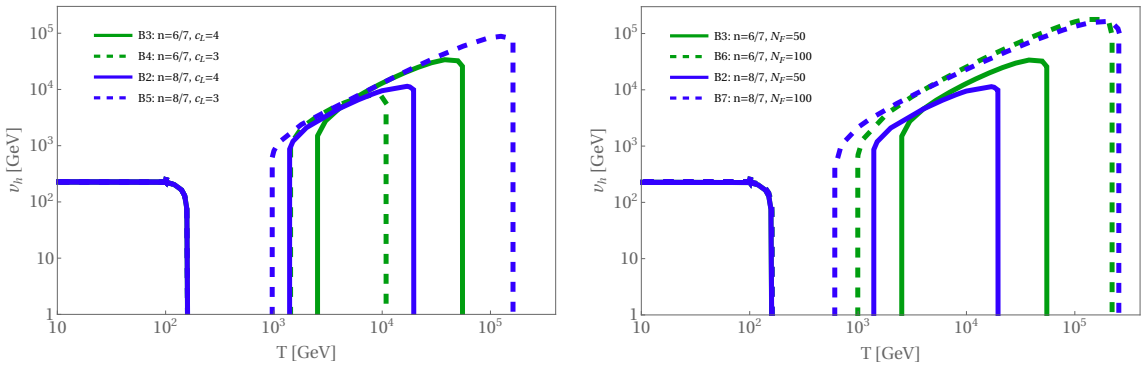

Figure 4.4: Relationships between model parameters and features of thermal histories for nonlinear $s(T)$. **Left**: As c_L decreases, if $n > 1$ ($n < 1$), the lower temperature limit decreases (decreases), the upper temperature limit increases (decreases), and the duration of EW broken phase increases (decreases). B3 and B4, B2 and B5 only differ in c_L. **Right**: As N_F increases, both v_h/T and the duration of EW broken phase increase. B3 and B6, B2 and B7 only differ in N_F.

shift downward. Thus, if $n < 1$, we expect both the lower and upper temperature limits of EW broken phase become smaller and the duration of EW broken phase becomes shorter; if $n > 1$, we expect the lower temperature limit to decreases, the upper temperature limit to increases, and the duration of EW broken phase becomes longer.

In previous paragraphs, we implicitly assume c_1 and c_2 are independent of b_1, $y_{N'}$, and y_L because the thermal potential depends directly on m_i^2/T^2 (see Eq. (1.3)) and b_1, $y_{N'}$, y_L only affect the thermal potential via the masses of new fermions. On the other hand, the thermal potential also explicitly depend on N_F. Thus, we expect c_1 and c_2 depend on N_F. As explained in Section 1.1 and Section 2.3, the thermal effects from light new fermions (f_1; $f = N, E$) tend to break the EW symmetry, while the thermal effects from heavy new fermions (f_2) tend to restore the EW symmetry. If m_1/T, $m_2/T \ll 1$, the EW symmetry breaking thermal effects from f_1 are cancelled completely by f_2. However, the thermal effects are exponentially suppressed as m_i/T increases (see Eq. (1.4)), thus the cancellations from f_2 reduces significantly as $m_2/T \gg 1$, making fermion-induced EWSNR possible. c_2 corresponds to the

largest cancellations from f_2 allowed by fermion-induced EWSNR per generation of new fermions; i.e. if $m_2/T < c_2$, the cancellations from f_2 are too large, hence no fermion-induced EWSNR. c_1 is the upper bound of m_1/T that corresponds to the smallest contributions from f_1 per generation that are required to successfully induce EW symmetry breaking. As N_F increases, more cancellations from f_2 can be tolerated, while less contributions from f_1 per generation are required for fermion-induce EWSNR, hence we expect c_2 to decrease and c_1 to increase. Also, the $m_{N'}/T$ and m_L/T curves are independent of N_F. Therefore, when N_F increases, the lower temperature limit (upper temperature limits) decreases (increases) and the duration of EW broken phase increases (see Figure 4.4).

When comparing B7 to B2 (B6 to B3) in Figure 4.4, we also see that v_h/T increases at each T during the EW broken phase. Besides N_F, λ_2, $y_{NN'1}$, $y_{N'}/y_L$, g_2, and g' can also affect v_h/T. The full V_{eff} depends in a complicated fashion on (h_1, h_2, T) and the couplings, so it is impossible to obtain an anlytical expression for v_h/T. Nonetheless, we can gain some insights by focus only on the leading terms of V_{eff} in the high temperatures limit, i.e. assume

$$V_{\text{eff}}(h_2, T) \sim \frac{1}{4}\lambda_2 h_2^4 - \frac{a_h}{2}T^2 h_2^2 + \text{terms independent of } h_2\,, \tag{4.20}$$

where a_h is given by Eq. (2.23). In I2HDM+SSD model, when $T \gtrsim 160$ GeV, $\langle h_1 \rangle = 0$, thus

$$v_h = \langle h_2 \rangle \sim T\sqrt{\frac{a_h}{\lambda_2}}\,. \tag{4.21}$$

Thus, we expect v_h/T to increase when λ_2 decreases (or when a_h increases). As examples, Figure 4.5 shows how v_h/T changes as λ_2 and $y_{NN'1}$ varies. The plots are consistent with Eq. (4.21) qualitatively, but obviously not quantitatively. Eq. (4.20) not only ignore all the higher order corrections, but also implicitly assume $m_{f1}^2/T^2 \ll$

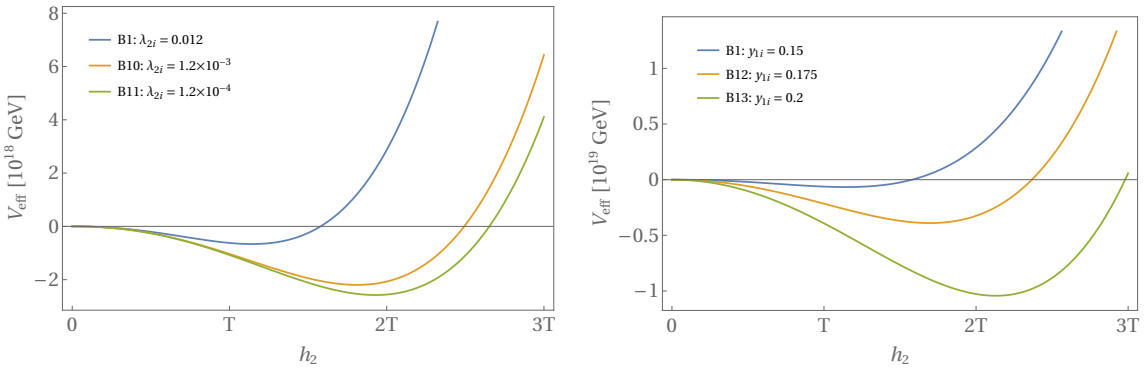

Figure 4.5: Relationships between model parameters and v_h/T. The model parameters of B10-B13 are exactly same as B1, except λ_2 (in left panel) or $y_{NN'1}$ (in right panel). Here, $T = 10^5$ GeV and the legends show the values of couplings at initial renormalization scale $\mu_0 = 173$ GeV. **Left**: v_h/T increases as λ_2 decreases. **Right**: v_h/T increases as $y_{NN'1}$ increases. $y_1 \equiv y_{NN'1}$.

1 (i.e. the assumption required for Eq. (1.5), which is not true for all the benchmarks shown in Figure 4.5. Thus, Eq. (4.21) overestimates v_h/T. Furthermore, the left panel of Figure 4.5 shows that v_h/T is not inversely proportional to $\sqrt{\lambda_2}$. By using the values of λ_{2i} shown in the legend of Figure 4.5 (left panel), Eq. (4.21) predicts that v_h/T of B11 (B10) is ten (three) times larger than v_h/T of B1, but the actual v_h/T of B10 and B11 are only about two times larger than v_h/T of B1. Also, although λ_{2i} of B11 is ten times smaller than λ_{2i} of B10, v_h/T of B11 is only slightly larger than v_h/T of B10. These discrepancies are due to the RG evolution of λ_2 induced by the EW gauge couplings (see $\beta(\lambda_2)$ in region C given in Chapter 3). As shown in the left panel of Figure 4.6, λ_2 increases as T increases; at initial renormalization scale, λ_2 of B11 is 10 (100) times smaller than λ_2 of B10 (B1), but when $T = 10^5$ GeV, λ_2 of B10 is only slightly larger than λ_2 of B11, and λ_2 of B1 is only about two times larger than λ_2 of B11. By using the values of λ_2 at ($T = 10^5$ GeV, $h_2 \sim T$), the estimations of v_h/T from Eq. (4.21) have the right order of magnitudes. For the same reason, benchmarks with $\lambda_{2i} < y^2_{NN'1i}/2$ can still have stable vacuum; B11 and B13 are examples of such cases (see right panel of Figure 4.6). Another consequence is

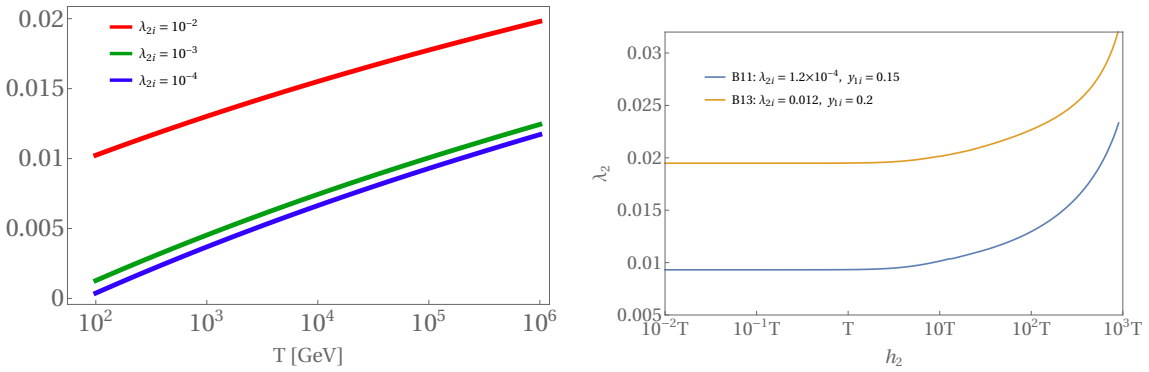

Figure 4.6: **Left**: λ_2 rises when temperature increases as a consequence of one-loop radiative corrections due to EW gauge couplings. Here, $h_1 = h_2 = 0$. The legend shows the values of couplings at initial renormalization scale $\mu_0 = 173$ GeV. **Right**: In B11 and B13, $\lambda_2 > 0$ within the parameter space of interest, albeit $\lambda_{2i} < y^2_{NN'1i}/2$. $T = 10^5$ GeV.

we cannot have benchmarks with v_h/T much larger than 1 in the allowed parameter space at temperatures well above 100 GeV. In Section 4.2.1, we will consider a more general SSD model that allow benchmarks with $v_h/T \gg 1$. These benchmarks may be probed by the future gravitational wave experiments (see Chapter 5).

4.2.1 Benchmarks with $v_h/T \gg 1$

Up to now, I have assumed new fermions of all N_F generations couple to the new real scalar σ and the inert Higgs Φ_2 with the same sets of yukawa couplings: y_L, $y_{f'}$, $y_{ff'i}$ ($f = N, E$, $i = 1, 2$). Also, I set $m_{X0} = 0$ ($X = N', E', L$) for simplicity's sake. However, a more general assumption is different generations of new fermions couple to σ and Φ_2 with different sets of yukawa couplings, and $m_{X0} \neq 0$. In fact, we can avoid the problem stated at the end of previous section by extending the previous I2HDM+SSD model with N_{F0} generations of SSD new fermions that only couple to Φ_2 and do not couple to σ. Also, their must have nonzero $m_{\tilde{X}0}$ ($\tilde{X}$: the additional new fermions) in order to satisfy the collider constraints stated in Section 4.1.1. I will label this new model as I2HDM+SSD+F0.

In I2HDM+SSD, λ_2 rises as T increases in region C and B because the heavy new

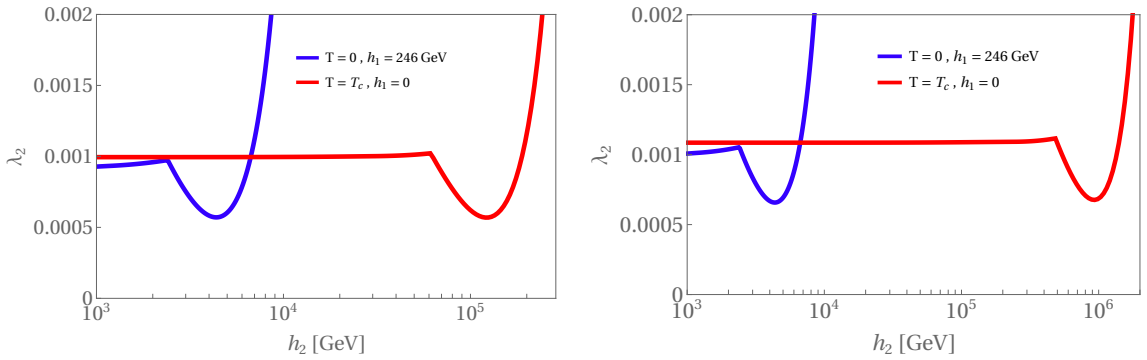

Figure 4.7: Evolution of λ_2 for benchmark S1 (**Left**) and S2 (**Right**) at $T = 0$ and $T = T_c$.

Table 4.2: Input parameters and couplings at initial renormalization scale $\mu_0 = 173$ GeV for benchmark S1 and S2, and their T_c, v_h/T_c. Both use $N_F = 100$, $y_{NN'1i} = 0.125$, $y_{Li}b_0 = 300\,\text{GeV}$, $N_{F0} = 1$, $y_{\tilde{f}\tilde{f}'i} = 0.415$, $m_{\tilde{X}0} = 200$ GeV.

	n	$y_{N'i}$	y_{Li}	b_1	λ_{2i}	T_c	v_h/T_c	T_n	v_h/T_n
S1	6/7	0.05	0.1	$80.4\,\text{GeV}^{1/7}$	9.8×10^{-4}	2.86 TeV	5.8	0.93 TeV	8.5
S2	8/7	0.1	0.2	$7.3\,\text{GeV}^{-1/7}$	9×10^{-4}	10.9 TeV	6.2	0.87 TeV	8.5

fermions are decoupled and the positive g_2, g' terms in $\beta(\lambda_2)$ dominate. To suppress the growth of λ_2 in region C and B, we choose $m_{\tilde{X}0} = 200$ GeV and $y^2_{\tilde{f}\tilde{f}'i} > 2\lambda_2$. These new fermions have temperature-independent masses, since they do not couple to σ. Thus, they will not decouple in region C and B, and their negative contributions to $\beta(\lambda_2)$ partially cancel the positive contributions from g_2, g'. In benchmarks S1 and S2, only one new generation and $y_{\tilde{f}\tilde{f}'i} = 0.415$ are sufficient to achieve large v_h/T (see Table 4.2). As shown in Figure 4.7, $\lambda_2 \approx \lambda_{2i}$ in region B and C from $T = 0$ to T_c (the upper temperature limit of EW broken phase). Note that $\lambda_2 > 0$ in the parameter space of interest, so S1 and S2 have stable vacuum. Table 4.2 also show their v_h/T ratio at nucleation temperature T_n. As we shall see in Chapter 5, the key parameters of gravitational wave signal calculations are evaluated at $T = T_n$, so v_h/T_n is related to the strength of of gravitational wave signals, not v_h/T_c.

Chapter 5

Gravitational wave signals

Gravitational waves (GWs) can be produced from time-varying distributions of energy-momentum and they propagate away from their sources indefinitely, in analogy with the production of electromagnetic waves from time-varying charge distributions, but in contrast to the massive $W^{\pm}$ and Z^0 bosons generated by weak interactions that decay promptly, and gluons radiated from strong interactions that immediately hadronize. Thanks to the long range nature of GWs, we can learn about the history of universe during its infancy by detecting the GWs that are generated in the early universe, similar to how the detection of cosmic microwave background (CMB) revolutionize our cosmology knowledge. Some examples of well-motivated cosmological sources for GWs are inflation, cosmic strings, and first order phase transitions (FOPTs) [48]. In Chapter 4, it is shown that our models predict FOPTs when $s(T)$ (VEV of the scalar field that control the new fermions' masses) is nonlinear. Furthermore, there exists parameter space where strong FOPT can occur while satisfying all constraints. However, as explained in [49, 50], successful FOPT also requires the true-vacuum bubbles nucleation rate to be at least of the same order as H^4 (H is the Hubble parameter) in order to be consistent with the Big Bang Nucleosynthesis theory (see review in [51]) and the fact that universe is homogeneous and isotropic (one of the strong evidences is the uniformity of CMB temperature across the sky). In Section 5.1, I will explain

how the bubbles nucleation rate and other key parameters that characterize FOPT are computed from underlying field models. Then, those key parameters will be used to calculate the spectra of GWs in Section 5.2. In Section 5.3, I will present the GW signal predictions of our models and assess their discovery potential in several future GW experiments.

5.1 Determining the properties of FOPT by the models of elementary particles

By definition, first order EW phase transition occurs if the EW VEV changes discontinuously at some temperature. A necessary condition is the effective potential of the electroweak sector must have degenerate minima at some temperature (known as the critical temperature T_c). For example, in Figure 5.1, when the temperature is above $T_c = 2.86$ TeV, the universe is in EW symmetric phase since the global minimum of V_{eff} is 0, but the global minimum jumps to some nonzero value when the temperature drops below T_c. However, just because the global minimum of V_{eff} changes discontinuously at $T = T_c$ does not mean FOPT will complete instantenously at $T = T_c$. In this example, FOPT actually begins around $T_n = 0.93$ TeV when the decay rate from the metastable state (also known as the false vacuum; it is $(h_1, h_2) = (0, 0)$ in this case) to another deeper minimum (usually the global minimum, also known as the true vacuum) is sufficiently large. The transition from false vacuum to true vacuum can occur via quantum tunneling and thermal fluctuations. The transition rate per unit volume (or nucleation rate) is given by

$$\Gamma = A(T)\, e^{-S(T)} \tag{5.1}$$

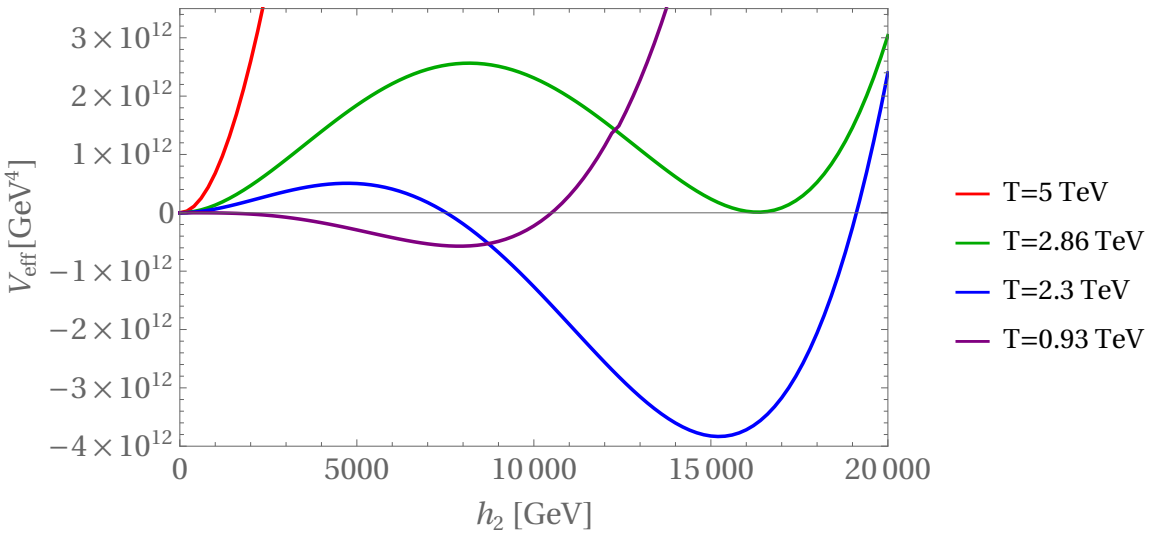

Figure 5.1: An example of first order EW phase transition. The critical temperature is $T_c = 2.86$ TeV and the true-vacuum bubbles nucleate around $T = 0.93$ TeV. $\langle h_1 \rangle = 0$ for all temperatures, so it is not displayed here.

where $S(T) = \min\{S_4[\phi_b], S_3[\phi_b]/T\}$ is known as the bounce action [52, 53]. S_4 and S_3 are the euclidean actions

$$S_n[\phi] = \int d^n x \left(\frac{1}{2} \partial_\mu \phi \partial_\mu \phi + V_{\text{eff}}(\phi, T) \right) , \tag{5.2}$$

and $\phi_b = \phi_b(r)$ are the $O(4)$ (or $O(3)$) symmetric field configuration that minimize S_4 (or S_3), under the boundary conditions

$$\lim_{r \to \infty} \phi_b(r) = \phi_+ \quad \phi'(0) = 0 \quad \phi(0) = \phi_- . \tag{5.3}$$

ϕ_+ and ϕ_- are the false and true vacuum respectively. Thus, the bounce solution ϕ_b describes a "true-vacuum bubble" (i.e. spherically symmetric) that has the value of ϕ_- at its center and surrounded by the false vacuum ϕ_+ at infinity. Since the corresponding Euler-Lagrange equation is a second-order differential equation, there are situations in which the three boundary conditions in Eq. (5.3) cannot be simultaneously satisfied. In those cases, the third condition can be relaxed; physically, it

means the false vacuum does not necessarily decay into the global minimum of V_{eff}. We use the numerical package **FindBounce** to calculate the bounce action [54].

The prefactor $A(T)$ in Eq. (5.1) is usually difficult to compute. At finite temperature, when the thermal fluctuations dominates the quantum fluctuations (i.e. $S(T) = S_3/T$, which is true for our cases), $A(T)$ can be formally expressed as [53, 55, 56]

$$A = \frac{\omega_-}{\pi}\left(\frac{S_3}{2\pi T}\right)^{3/2}\left(\frac{\det' K[\phi_b]}{\det K[\phi_+]}\right)^{-1/2} \tag{5.4}$$

$$K \equiv \frac{\delta^2 S}{\delta\phi^2}\,. \tag{5.5}$$

$K[\phi_b]$ have three zero eigenvalues that correspond to the three translational symmetries of S_3 broken by the bounce ϕ_b. They are removed when evaluating the determinant (denoted by $\det' K$) and replaced by "normalization factor" $\left(\frac{S_3}{2\pi T}\right)^{3/2}$. ω_- describes the growth rate of the critical bubble, and the ratio of the functional determinants describes the thermal and quantum fluctuations about the critical bubble. As pointed out in [57], A cannot be calculated from first principles within the standard framework that we adopted in this paper: first, V_{eff} is calculated by expanding the effective action around the zero external momenta configurations, so V_{eff} depends only on the homogeneous scalar background fields; then, V_{eff} is used again to calculate the bounce $\phi_b(r)$, bounce action $S[\phi_b]$, and prefactor $A[\phi_b]$. However, ϕ_b must be inhomogeneous by nature, contradicts with the first step. Nonetheless, here we are interested in the cases that have strong FOPT, which requires λ_2 to be much smaller than the new yukawa couplings, so we expect this standard framework gives good estimations. Here, we will use the simple dimensional estimates $A(T) = T^4$. Some papers also choose $A(T) = \alpha_w^5 T^4$ because the characteristic time and distance of the non-abeliean gauge fields fluctuations scale as g^4T and g^2T respectively when the non-perturbative dynamics dominates [58–61]. However, the results in [57] indi-

cate that this choice is probably incompatible with our framework. Fortunately, as shown in Section 5.3, S_3/T is linear in T around $T = T_n$ and $T_n S_3'(T_n) \gtrsim 200$ for all cases, thus the nucleation rate and nucleation temperature are much more sensitive to the calculation of S_3/T. For example, the error in A (i.e $\delta A/A$) need to be larger than about $e^{20.8}$ in order to shift the temperature by 10%.

Now, we can use the bounce action and nucleation rate to compute the key parameters of FOPT $(T_n, \beta/H, \alpha)$, which later will be used to determine the GW spectra in Section 5.2. First, we need to define the temperatures at which the parameters are evaluated. Let T_* be the temperature of the thermal bath when the GWs are generated. Let T_n be the nucleation temperature, which is defined here as the temperature when $\Gamma(T_n) = H^4(T_n)$ (H is the Hubble parameter). It is the starting point of a successful FOPT (FOPT with a nucleation rate much less than H^4 is inconsistent with the experimental observations as mentioned above). When FOPT occur in vacuum-dominated epoch (e.g. as predicted in models with nearly conformal symmetry [62, 63]), the universe can be reheated (i.e. the free energy released from the false vacuum is converted into radiation [64–66]) to a temperature (denoted as $T_{\rm reh}$) that is much higher than T_n. In such case, $T_* \approx T_{\rm reh} \gg T_n$, so it is required to know $T_{\rm reh}$. In our cases, the phase transitions are completed in radiation-dominated epoch and the energy released from the false vacuum is small compared to the thermal energy of the primordial plasma, so typically $T_n \approx T_{\rm reh} \approx T_*$. Thus, the key parameters of FOPT can be evaluated at $T = T_n$ in our numerical studies. Finding T_n by using the definition $\Gamma(T_n) = H^4(T_n)$ can be time-consuming because it requires us to calculate the bounce action S_3/T as a function of temperature. In order to calculate S_3/T at each temperature, we need to find ϕ_- by minimizing $V_{\rm eff}$ and numerically solve for the bounce ϕ_b. Thus, before solving $\Gamma(T_n) = H^4(T_n)$, it is wise to estimate $S_3(T_n)/T_n$

by using

$$S_3(T_n)/T_n \approx 4\log(M_P/T_n) - 2\log\left(\frac{8\pi^3}{90}d_{\text{eff}}\right) \tag{5.6}$$

where $M_P = 10^{19}\,\text{GeV}$ is the Planck scale and d_{eff} is the effective degrees of freedom of relativistic particles in the plasma (see Eq. (4.15)). Since this estimation depends on $\log T_n$ only, a reasonable guess of T_n can estimate $S_3(T_n)/T_n$ well (of course it still requires us to know T_c and roughly how far T_n is below T_c, but it is easy to calculate T_c and the order of magnitude of T_n/T_c will be clear after studying a few benchmarks). Knowing $S_3(T_n)/T_n$ can help us to greatly narrow down the temperature interval that contains T_n, therefore we only need to calculate S_3/T for a small range of temperatures.

The time scale for the duration of FOPT is given by the β^{-1} [50], where

$$\beta \equiv -\frac{dS}{dt}\Big|_{t=t_n} = HT\frac{dS}{dT}\Big|_{T=T_n}. \tag{5.7}$$

The second equation is obtained by using $\dot{T} = -HT$, assumming the universe was radiation dominated at $T = T_n$. For example, the amount of time for the universe to go from $1 - e^{-0.01} \approx 1\%$ true vacuum to $1 - e^{-5} \approx 99\%$ true vacuum is roughly $\log(5/0.01)\beta^{-1} = 6\beta^{-1}$ (see Eq. (5.4) in [50];it is valid in our cases because $\beta/H(T_n) \gtrsim 200 \gg 1$, as shown in Section 5.3). In the next section, we will see that $\beta/H(T_n)$ affects both the peak frequency and the peak amplitude of spectrum of GW generated by FOPT.

The peak amplitude of GW spectrum also depends on the strength of the phase transition that is quantified by the parameter α. Essentially, it is a measure of the amount of energy (per unit volume) released from the false vacuum to the true vacuum compared to the energy density of the false vacuum. In the following, we will assume the false vacuum is in the symmetric phase (i.e. $\phi_+ = 0$) and the true vacuum is in

the broken phase. Also, the energy density of the false vacuum is dominated by the thermal bath of relativistic particles. These are valid assumptions for the scenarios that will be discussed in Section 5.3. In our numerical studies, we used the more general definition of α that is given in [67]:

$$\alpha \equiv \frac{\epsilon_+ - \epsilon_-}{b_+ T^4}\Big|_{T=T_*}, \tag{5.8}$$

where $\epsilon_\pm$ and $b_\pm$ are defined by

$$b_\pm \equiv \frac{3}{4T^3}\frac{\partial p_\pm}{\partial T}, \tag{5.9}$$

$$\epsilon_\pm \equiv \frac{1}{4}(\rho_\pm - 3p_\pm), \tag{5.10}$$

$$p_\pm = p_{eq} - V_{\text{eff}}(\phi_\pm, T), \tag{5.11}$$

$$\rho_\pm = T\frac{\partial p_\pm}{\partial T} - p_\pm, \tag{5.12}$$

$$p_{eq} \equiv \sum_i \frac{d_i}{6\pi^2}\int_{m_i}^{\infty} dE \frac{(E - m_i^2)^{3/2}}{e^{E/T} - a_i}. \tag{5.13}$$

ϕ_+ and ϕ_- are the false and true vacuum respectively and a_i, d_i m_i are defined in Chapter 1. The equations above implicitly assume the early universe primordial plasma and the vacuum state are in thermal equilibrium and interactions among the particles in the plasma are negligible. Thus, the pressure of plasma is given by Eq. (5.13) and the total pressure ($p_\pm$) equals to the sum of the plasma's pressure (p_{eq}) and the pressure from vacuum state ($-V_{\text{eff}}$) (Eq. (5.11)). Then, the total energy density $\rho_\pm$ can be obtained from the total pressure by the thermodynamic relation Eq. (5.12) (since Gibbs free energy is minimized). If the particle i is relativistic ($m_i \ll T$) or non-relativistic ($m_i \gg T$), its $p_{eq,i}$, $\rho_{eq,i}$ have much simpler forms:

$$\text{relativistic:} \quad \rho_{eq,i} = \frac{\pi^2}{30} d_i T^4, \qquad p_{eq,i} = \rho_{eq,i}/3, \tag{5.14}$$

$$\text{non-relativistic:} \quad \rho_{eq,i} = \frac{d_i}{(2\pi)^{3/2}} \left(\frac{m_i}{T}\right)^{5/2} e^{-m_i/T}\, T^4, \quad p_{eq,i} = (T/m_i)\rho_{eq,i}\,. \tag{5.15}$$

At high temperature, the energy density and pressure of non-relatvistic particles are usually negligible compared to the relativistic particles in the plasma because of small factor $e^{-m_i/T}$, unless degrees of freedom of the non-relativistic particles are much larger than those of relativistic particles. Thus, when the plasma contains only the relativistic (rel.) and non-relativistic particles, $b_\pm$ becomes temperature-independent and $\epsilon_\pm$ depends on V_{eff} only:

$$b_\pm = \frac{\pi^2}{30} d_{\text{eff}}\,, \tag{5.16}$$

$$\epsilon_\pm = V_{\text{eff}}(\phi_\pm, T) - \frac{1}{4} T\, \partial_T V_{\text{eff}}(\phi_\pm, T)\,. \tag{5.17}$$

However, as can be seen from the discussion in Chapter 2, some of the new fermions in our model are neither relativistic nor non-relativistic (depending on the parameter space) and they contribute significantly to the total energy density and pressure at high temperature due to their large degrees of freedom ($d_{Ni} = d_{Ei} = 4N_F$). Thus, it is necessary to use the more general definitions of $b_\pm$ and $\epsilon_\pm$ (Eq. (5.9),(5.10)) to calculate α in our cases.

Besides T_n, α, and β, the GW spectra also depend on the velocity of bubble wall v_w (or α_∞) and the efficiency factors (κ_{sw}, κ_{col}, κ_{turb}) associate with different GW production mechanism. These parameters will be introduced along with the major production mechansims of GWs in the next section.

5.2 GW spectra from FOPT

During the FOPT, there are three possible production mechanisms of gravitational waves: collisions of true-vacuum bubbles (col), sound waves (sw), and magnetohydro-

dynamics (MHD) turbulence (turb) in primordial plasma. I will first briefly describe each mechanism and then summarize the formula we used for calculating the GWs spectra (Eq. (5.19)-(5.29)).

In Section 5.1, we see that a true-vacuum bubble (in vacuum-dominated epoch) which is described by the bounce solution ϕ_b has $O(4)$ symmetry. Just by symmetry consideration, one can show that the bubble wall will accelerate outward and approach the speed of light very quickly. However, also because of its symmetry, a single bubble cannot produce GW according to Birkhoff's theorem. The collisions of two or more bubbles will break such symmetry and generate GWs (the breaking of the $O(2,1)$ symmetry of two bubbles is more subtle, as explained in [68]). Thus, collision of bubbles is the simplest possible GWs production mechanism during FOPT. But even in this simplest case, the calculations of GWs production have to be done numerically and efficient numerical simulations requires certain approximations. [69] found that the "envelope approximation" works very well: the energy-momentum tensor is calculated by considering only the portion of bubbles' surface that remains uncollided (i.e. the "envelope" of all bubbles) and assume the bubble walls are thin. If the GWs are generated during the vacuum-dominated epoch, bubbles collision is the only dominant production mechanism since the plasma is negligible. In other situations, the primordial plasma plays a crucial role in GWs production.

At high temperature, the evolution of the bubble wall depends strongly on the fluid dynamics of the primordial plasma. It can be studied via cosmic fluid-order parameter field model [70, 71] and relativistics hydrodynamics [67]. During a FOPT, the energy liberated from false vacuum (also known as latent heat) will accelerate the bubble wall of the true vacuum, but the friction from the hot plasma will resist the expansion and decelerate the bubble wall to a terminal speed. Through this interaction between the bubble wall and the plasma, typically (the precise condition will be given below) most of the latent heat will be transferred from the bubble into

the plasma, in contrast to the first mechanism in which most of the latent heat is stored in the bubble walls before bubble collisions. Most of the energy absorbed by the plasma goes into the thermal energy of the plasma and only a small fraction of the energy transforms into the bulk kinetic motions (i.e. sound waves) that generate the GWs. [67] studied the numerical solutions of the fluid equations in detail, and obtained the efficiency factor $\kappa_{\rm sw}$ as a function of the strength of phase transition α and the bubble wall speed v_w (appendix A in [67] uses different notations: κ, α_N, ξ_w). In our numerical studies, for each α, we will use this function to find the maximum $\kappa_{\rm sw}$ and the corresponding v_w (in principle, κ can also be calculated from the microscopic physics model, but some additional assumptions about the friction in plasma are required). We found that $\kappa_{\rm sw} \sim \mathcal{O}(0.1)$ even for the benchmark with the strongest FOPT ($\alpha \sim 0.01$) and it is the supersonic deflagrations region that give the maximum efficiencies (supersonic deflagration is the hybrid mode of deflagration (when $v_w < c_s$) and supersonic mode (when $v_w > c_s$); c_s is the speed of sound in the plasma).

If the strength of a FOPT is sufficient strong, the energy released from the false vacuum during the phase transition may overcome the friction in the plasma and cause the true-vacuum bubbles to accelerate continuously and "run away" with $v_w \to c$. To distinguish this case from the previous case, we need to compare α with a parameter that can descibe the friction in the plasma. According to Section 6 of [67], the appropriate parameter is

$$\alpha_\infty = \frac{1}{b_+} \sum_i \frac{d_i \Delta\eta_i^2}{4\pi^2 T_*^2} \int_{\eta_{i,+}}^\infty dy \frac{(y^2 - \eta_{i,+}^2)^{1/2}}{e^y - a_i}\,, \tag{5.18}$$

$$\eta_{i,\pm} \equiv m_i(\phi_\pm)/T\,, \quad \Delta\eta_i^2 \equiv \eta_{i,-}^2 - \eta_{i,+}^2\,.$$

$\Delta\eta_i^2$ factor in Eq. (5.18) captures an important feature of the friction exerted on the

bubble wall by the primordial plasma: the pressure difference (i.e. friction) along the bubble wall is generated mostly by the particles that become heavy during the phase transition. When $\alpha < \alpha_\infty$, no runaway bubble is allowed in the plasma, which is the case described in the previous paragraph. On the other hand, when $\alpha > \alpha_\infty$, the bubbles can run away, and only α_∞/α of the latent heat is absorbed by the plasma and the efficiency factor becomes $\kappa_{\rm sw}\alpha_\infty/\alpha$. The remaining energy goes into the bubble wall, hence $\kappa_{\rm col} = 1 - \alpha_\infty/\alpha$. In our cases, we found numerically that $\alpha < \alpha_\infty$ are always satisfied, so there is no runway bubble and sound waves is the dominant GW source.

As the bubble collisions "stir up" the plasma, turbulence is expected to be developed in the early universe because of its high Reynolds number ($\mathrm{Re}(L_*)$). In our cases, $T_n \sim \mathcal{O}(1-100)$TeV and $L_* \sim v_w\beta^{-1}$, thus $\mathrm{Re}(L_*) \gtrsim 10^{10}$ (using the estimation method given in Section 3.5 of [72]). The high conductivity of the hot plasma ($\sigma \approx T/(\pi e^2)$) implies that its magnetic Reynolds number is also very large (see appendix B in [72]), thus the turbulence in hot plasma should be studied by using MHD [73,74]. In contrast to the bubble collisions mechanism, the production of GWs from MHD turbulence does not cease immediately after the phase transtion ends. The dissipation of MHD turbulence requires several Hubble times due to the large $\mathrm{Re}(L_*)$ of hot plasma in the early universe. This characteristics is reflected in Eq. (5.29) as an enhancement of its GW spectrum amplitude by a factor of β/H_* with respect to the short-lasting sources (bubble collisions; Eq. (5.27)). The sound wave discussed in the previous paragraphs is also a long-lasting source of GWs with the effective lifetime $\sim \mathcal{O}(H_*^{-1})$ because the sound waves in the plasma (initiated by motions of the bubble walls) continue to oscillate even after the bubble walls were destroyed by collisions among the bubbles. This is confirmed by numerical simulations [71]. However, in the same study, it was found that only $5\% - 10\%$ of the fluid bulk motion is turbulence. This is not surprising because the numerical simulation were performed for $\alpha \lesssim 0.1$,

and its results are applicable for our cases (our model predicts $\alpha \lesssim 0.01$). Thus, we use the conservative choice $\kappa_{\rm turb} = 0.05\kappa_{\rm sw}$ in our numerical calculations. Moreover, in [73], it was found that the efficiency of GW production sourced from MHD turbulence is very sensitive to the mechanism that initiate the plasma pertubations. Thus, accurate prediction of $\kappa_{\rm turb}$ requires deeper understanding of how the latent heat of a given model is distributed between the magnetic field and primordial plasma (e.g. magnetogenesis in the strong EWPT was studied in [75]).

In summary, the relative contributions of these mechanisms can vary a lot depending on the epoch when GWs are generated, the strength of FOPT α, and the particle species in the primordial plasma (characterized by α_∞). In vacuum-dominated epoch (VD), GWs are produced dominantly via collisions of bubbles. If the GWs are generated during the radiation-dominated epoch (RD), there are two qualitatively distinctive cases, distinguished by whether there are runaway bubbles in the plasma or not. If there is no runaway bubble ($\alpha < \alpha_\infty$), sound wave is the dominant source of the GWs; if runaway bubbles are allowed ($\alpha > \alpha_\infty$), both the sound waves and bubble collisions can be important sources. The contribution from bubble collisions increases as α/α_∞ increases, and it is equivalent to the VD case when $\alpha \gg \alpha_\infty$. If GWs is generated during or before an early matter-dominated epoch (MD), the GW signals is generally smaller compared to the RD case [76]. Our cases are best described by the RD category without runaway bubble.

For the RD case, the energy density contained in GWs per logarithmic frequency interval, normalized to the critical energy density of the universe today is given by (see [77]):

$$\begin{aligned} &\Omega_{\rm GW,RD} = \Omega_{\rm col} + \Omega_{\rm sw} + \Omega_{\rm turb}\,, \\ &\Omega_j = S_j(f, f_j)\,\tilde{\Omega}_j(T_*, \alpha, \beta/H_*, v_w, \kappa_j)\,, \quad \text{(j=col, sw, turb)}\,. \end{aligned} \tag{5.19}$$

(To pe precise, $\rho_{GW}/\rho_c \equiv \int_0^\infty d\log f\, \Omega_{GW}(f)$, where ρ_{GW} is the energy density of the GWs and $\rho_c = 3H_0^2/(8\pi G)$ is the critical energy density of the universe today [78].) In Eq. (5.19), S_j describes the shape of GW spectrum of contribution j. S_j depends explicitly only on frequency f and peak frequency f_j ($S_{\rm turb}$ also depends explicitly on f_{*0} (see Eq. (5.22)) essentially because it is a long-lasting source [72, 79]). On the other hand, the peak amplitude of GW spectrum $\tilde{\Omega}_j$ depends explicitly on the model-dependent key parameters α, β/H_*, v_w. In Section 5.3, we will see how this feature of Ω_j can be utilized to simplify and improve the signal-to-noise analysis, making it much easier to compare the theoretical predictions with detectors' sensitivities [80].

The spectral shape functions of the three contributions are

$$S_{\rm col} = \left(\frac{f}{f_{\rm col}}\right)^{2.8}\left[\frac{3.8}{1+2.8(f/f_{\rm col})^{3.8}}\right], \tag{5.20}$$

$$S_{\rm sw} = \left(\frac{f}{f_{\rm sw}}\right)^{3}\left[\frac{7}{4+3(f/f_{\rm sw})^{2}}\right]^{7/2}, \tag{5.21}$$

$$S_{\rm turb} = \left(\frac{f}{f_{\rm turb}}\right)^{3}\left[\frac{1}{1+(f/f_{\rm turb})}\right]^{11/3}\frac{2^{11/3}\,(1+8\pi f_{\rm turb}/h_*)}{1+8\pi f/f_{*0}}, \tag{5.22}$$

where the peak frequencies and f_{*0} are given by

$$f_{\rm col} = 1.65\,{\rm Hz}\left(\frac{d_{{\rm eff}\,*}}{100}\right)^{1/6}\left(\frac{T_*}{1\,{\rm TeV}}\right)\left(\frac{\beta/H_*}{100}\right)\left(\frac{0.62}{1.8-0.1v_w+v_w^2}\right), \tag{5.23}$$

$$f_{\rm sw} = 0.19\,{\rm Hz}\left(\frac{d_{{\rm eff}\,*}}{100}\right)^{1/6}\left(\frac{T_*}{1\,{\rm TeV}}\right)\left(\frac{\beta/H_*}{100}\right)\left(\frac{0.1}{v_w}\right), \tag{5.24}$$

$$f_{\rm turb} = 0.27\,{\rm Hz}\left(\frac{d_{{\rm eff}\,*}}{100}\right)^{1/6}\left(\frac{T_*}{1\,{\rm TeV}}\right)\left(\frac{\beta/H_*}{100}\right)\left(\frac{0.1}{v_w}\right), \tag{5.25}$$

$$f_{*0} \equiv H_*\left(\frac{a_*}{a_0}\right) = 0.165\,{\rm mHz}\left(\frac{d_{{\rm eff}\,*}}{100}\right)^{1/6}\left(\frac{T_*}{1\,{\rm TeV}}\right). \tag{5.26}$$

The peak amplitudes of the GW spectra are

$$\tilde{\Omega}_{\rm col}h^2 = \frac{1.67\times10^{-5}}{(\beta/H_*)^2}\left(\frac{100}{d_{{\rm eff}\,*}}\right)^{1/3}\left(\frac{\kappa_{\rm col}\alpha}{1+\alpha}\right)^2\left(\frac{0.11v_w^3}{0.42+v_w^2}\right), \tag{5.27}$$

$$\tilde{\Omega}_{\rm sw}h^2 = \frac{2.65\times10^{-6}}{\beta/H_*}\left(\frac{100}{d_{\rm eff\,*}}\right)^{1/3}\left(\frac{\kappa_{\rm sw}\alpha}{1+\alpha}\right)^2 v_w\,, \tag{5.28}$$

$$\tilde{\Omega}_{\rm turb}h^2 = \frac{3.35\times10^{-4}}{\beta/H_*}\left(\frac{100}{d_{\rm eff\,*}}\right)^{1/3}\left(\frac{\kappa_{\rm turb}\alpha}{1+\alpha}\right)^{3/2} v_w\left(\frac{2^{-11/3}}{1+8\pi f_{\rm turb}/h_*}\right)\,, \tag{5.29}$$

where $H_* \equiv H(T_*)$, f_{*0} is the redshift of H_* to present day, and $h \equiv H_0/(100\,\mathrm{km/s/Mpc})$ where H_0 is the Hubble parameter today. $d_{\rm eff\,*}$ (defined in Eq. (4.15)) is the effective degrees of freedom of relativistic particles in true vacuum at $T = T_*$.

The typical benchmarks of our model that gives strong FOPT have $T_* \sim 1\,\mathrm{TeV}$, $\alpha \sim 0.01$, $\beta/H* \sim 100$, $v_w \sim 0.1$, $\kappa_{\rm sw} \sim 0.1$, $d_{\rm eff*} \sim 100$, hence we expect the GW spectra (mainly produced by sound waves) peak around $f_{\rm sw} \sim 0.1\,\mathrm{Hz}$, and the peak amplitude is about $\tilde{\Omega}_{\rm sw}h^2 \sim 10^{-15}$. This rough estimation suggests that future detectors like Big Bang Observer (BBO) and Deci-hertz Interferometer Gravitational wave Observatory (DECIGO) may be able to test our model (these detectors are most sensitive around 0.1 Hz. Other proposed future GW detectors like Laser Interferometer Space Antenna (LISA; most sensitive around 1 mHz), Einstein Telescope, Cosmic Explorer (most sensitive around 10 Hz) are not sensitive to our model. Our numerical GW signal predictions will be compared with sensitivity curves of BBO and DECIGO more carefully in the next section.

5.3 GW signal predictions and detection prospects

In Figure 5.2, we can see that the GW spectrum from sound waves increases as f^3 for low frequecies and decreases as f^{-4} for high frequencies, while GW spectrum from MHD turbulence increases as f^3 for low frequecies and decreases as $f^{-5/3}$ for high frequencies, but it rises slower in the intermediate frequecy range as f^2 due to causality and the fact that its active time can span several Hubble times (which is much longer than the phase transition period) [72, 79]. While GW spectrum plots

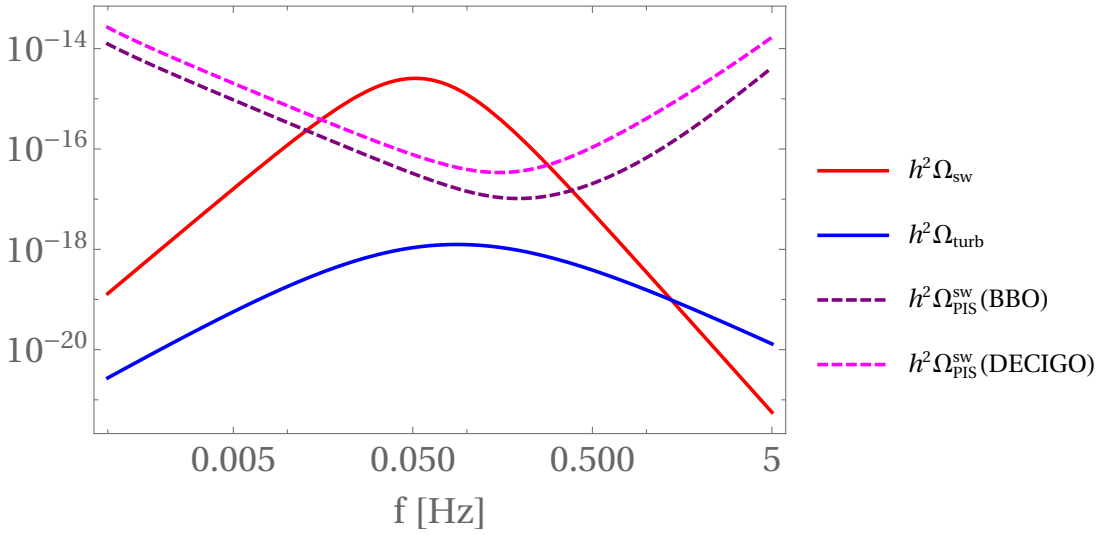

Figure 5.2: An example of GW spectra from different production mechanisms.

like Figure 5.2 convey some useful information about the predicted GW signals, it is not clear from such plots if the signals are detectable by the GW experiments. A GW signal is detectable by a detector if its signal-to-noise ratio (SNR) exceeds the SNR threshold (denoted as $\varrho_{\rm thr}$) of the detector. SNR is a quantity that compares the strength of a GW signal to the noise of a detector, which is defined as [81, 82]

$$\varrho \equiv \left[n_{\rm exp} t_{\rm exp} \int_{f_{\rm min}}^{f_{\rm max}} df \left(\frac{\Omega_{\rm GW}(f)}{\Omega_{\rm exp}(f)} \right)^2 \right]^{1/2} , \tag{5.30}$$

where $n_{\rm exp} = 1$ (2) for experiments that use auto-correlation (cross-correlation) measurements and $t_{\rm exp}$ is the total experimental observation period (see Table 5.1). $\Omega_{\rm GW}(f)$ can be calculated by the equations given in the previous section, while $\Omega_{\rm exp}(f)$ is the noise spectrum of the GWs detector. The GWs of cosmological origins will appear as stochastic background of gravitational waves signals because the universe is isotropic and homogeneous, and their sources are numerous and too far away to be angularly resolved by current and proposed future gravitational wave detectors. Usually, the published intrinsic noise spectra of GWs detectors (e.g. those that are available

Table 5.1: Properties of several future gravitational wave detectors [80, 83].

	$\varrho_{\rm thr}$	$t_{\rm exp}$ [yr]	$n_{\rm exp}$
BBO	10	4	2
DECIGO	10	4	2
LISA	10	4	1
CE	10	5	1
ET	5	5	2

on LIGO's Document Control Center dcc.ligo.org) are not same as the $\Omega_{\rm exp}(f)$ in the Eq. (5.30), as $\Omega_{\rm exp}(f)$ is noise spectrum for the measurements of stochastic gravitational wave background. [80] has explained in details how $\Omega_{\rm exp}(f)$ can be calculated from the available intrinsic noise spectra in its appendices. In next paragraph, I will explain how the peak-integrated sensitivity curves (PISCs) proposed in [80] can be used to easily and accurately visualize the SNR of GWs predictions.

We have already seen in Eq. (5.19) that the frequency-depencency of GW spectrum contained entirely in the spectral shape functions S_j, thus we can rewrite Eq. (5.30) as

$$\varrho = \left[\frac{t_{\rm exp}}{1{\rm yr}}\left(\sum_i \varrho_i^2 + \frac{1}{2}\sum_{i\neq j}\varrho_{i/j}^2\right)\right]^{1/2}, \tag{5.31}$$

$$\varrho_{i/j} \equiv \frac{\left(\tilde{\Omega}_i\tilde{\Omega}_j\right)^{1/2}}{\Omega_{\rm PIS}^{i/j}}, \quad \varrho_i \equiv \varrho_{i/i}\,, \tag{5.32}$$

$$\Omega_{\rm PIS}^{i/j} \equiv \left[n_{\rm exp}(1\,{\rm yr})(2-\delta_{ij})\int_{f_{\rm min}}^{f_{\rm max}} df\,\frac{S_i(f)S_j(f)}{\Omega_{\rm exp}^2(f)}\right]^{-1/2}, \tag{5.33}$$

where $i, j =$ col, sw, turb (the three different GWs production mechanisms explained in Section 5.2). Here, $\varrho_{i/j}$ are normalized to observation time of one year. $\Omega_{\rm PIS}^{i/j}$ is known as peak-integrated sensitivity, which describes the effecitive sensitivity of a detector with respect to GWs production mechanisms i and j. The computations of peak-integrated sensitivity curves (PISCs) (i.e. $\Omega_{\rm PIS}^{i/j}$ as functions of peak frequencies

Table 5.2: Model parameters for benchmark M1. M1 is based on the I2HDM+SSD+F0 model, with $N_{F0} = 1$, $y_{\tilde{f}\tilde{f}'i} = 0.415$, $m_{\tilde{X}0} = 200$ GeV.

N_F	$y_{N'i}$	y_{Li}	$y_{NN'1i}$	n	c_L	$y_{Li}b_0$	T_1	λ_{2i}	$-\mu_{2i}^2$
45	0.05	0.1	0.186	6/7	2.8	300 GeV	20 GeV	4×10^{-4}	$(50\,\mathrm{GeV})^2$

f_i, f_j, f_{*0}) only require us to know the noise spectrum of a detector and the spectral shapes, which do not rely on a specific particle physics model. Thus, once we constructed PISCs, we can use them to compute SNR of any models and parameter points straightforwardly by Eq. (5.31) and no additional frequency integration is required. In our cases, since the GWs are dominantly produced via sound waves, SNR is simply

$$\begin{aligned} \varrho &\approx \varrho_{\rm sw}\sqrt{t_{\rm exp}/(1\,{\rm yr})} = \frac{\tilde{\Omega}_{\rm sw}}{\Omega_{\rm PIS}^{\rm sw}}\sqrt{t_{\rm exp}/(1\,{\rm yr})}\,, \\ \Omega_{\rm PIS}^{\rm sw} &\equiv \left[n_{\rm exp}(1\,{\rm yr})\int_{f_{\rm min}}^{f_{\rm max}} df\left(\frac{S_{\rm sw}(f)}{\Omega_{\rm exp}(f)}\right)^2\right]^{-1/2} \end{aligned} \tag{5.34}$$

From now on, the labels "sw" will be omitted. Thus, in the cases when there is only one major GWs source, the calculation of SNR becomes trivial once we obtained the PISCs. Now we can plot the PISCs together with peak amplitudes of GW spectra $\tilde{\Omega}$ and see immediately if the predicted GW signals exceed the SNR thresholds of GW detectors. Figure 5.3 shows PISCs of BBO, DECOGO detectors and the gravitational wave signals of two benchmarks with stable vacuum (S1 and S2; see Table 4.2) and one benchmark with metastable vacuum (M1; see Table 5.2). Their signal-to-noise ratio all exceed $\varrho_{\rm thr}$ of BBO and DECIGO (see Eq. (5.34) and Table 5.1).

In M1, $\lambda_2 < 0$ for certain ranges of h_2 (see Figure 5.4), hence its effective potential has a deeper minimum in h_2 direction that is not the EW vacuum. To verify that the physical EW vacuum is indeed metastable, we numerically checked that $\Gamma \ll H^4$ at finite temperatures, and the tunneling probablity to the deeper minimum ($(h_1, h_2) =$

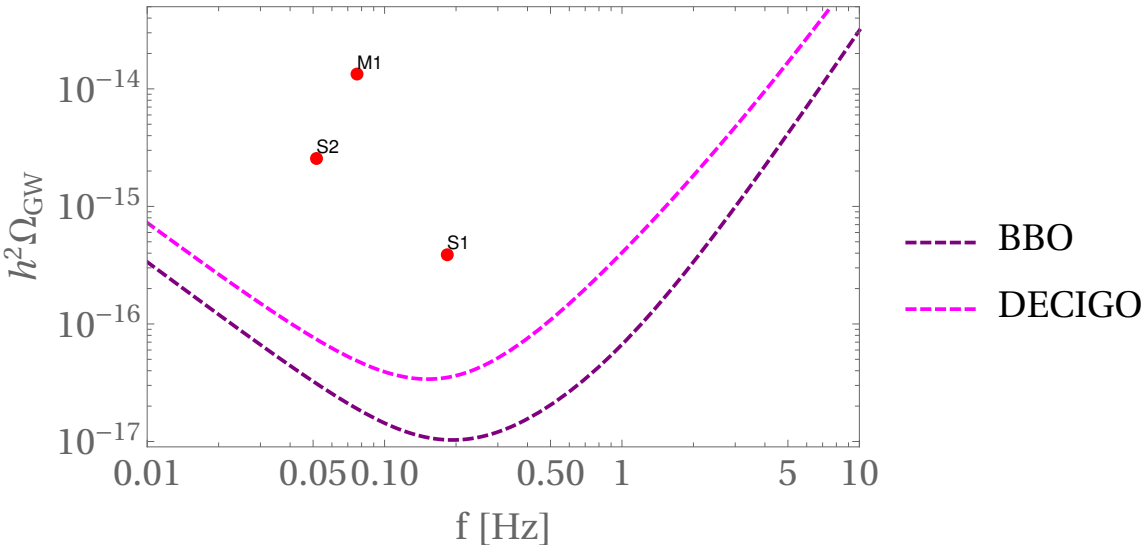

Figure 5.3: The dashed curves are PISC for BBO and DECIGO. The points are benchmarks S1, S2, M1 (see Table 4.2 and Table 5.2 for details). The x-coordinate of each benchmark is its peak frequencies, y-coordinate is its peak GW strength.

$(246\,\text{GeV}, 1.16\times10^5\,\text{GeV}))$ at $T=0$ is less than 1. On the basis of dimensional argument, the tunneling probability at $T=0$ is [32, 84]

$$\mathcal{P}_0 \sim \frac{\Lambda_B}{H_0^4} e^{-S_4}\,, \tag{5.35}$$

where H_0 is the Hubble constant at present time, and Λ_B is the characteristic energy scale associated with the bounce solution. Although there is some ambiguity about Λ_B, we will see shortly that it does not matter in this case. To have $\mathcal{P}_0 < 1$, we need

$$S_4 \gtrsim 386.8 + 4\left[\log(\Lambda_B/\text{GeV}) - \log(2.1\,h)\right]\,. \tag{5.36}$$

Thus, for $\Lambda_B \leq M_P$, $\mathcal{P}_0 < 1$ requires $S_4 \gtrsim 560$. The bounce action of M1 from $(246\,\text{GeV}, 0)$ to $(h_1, h_2) = (246\,\text{GeV}, 1.16\times10^5\,\text{GeV})$ is $S_4 = 6.25\times10^3$, hence $\mathcal{P}_0 \ll 1$.

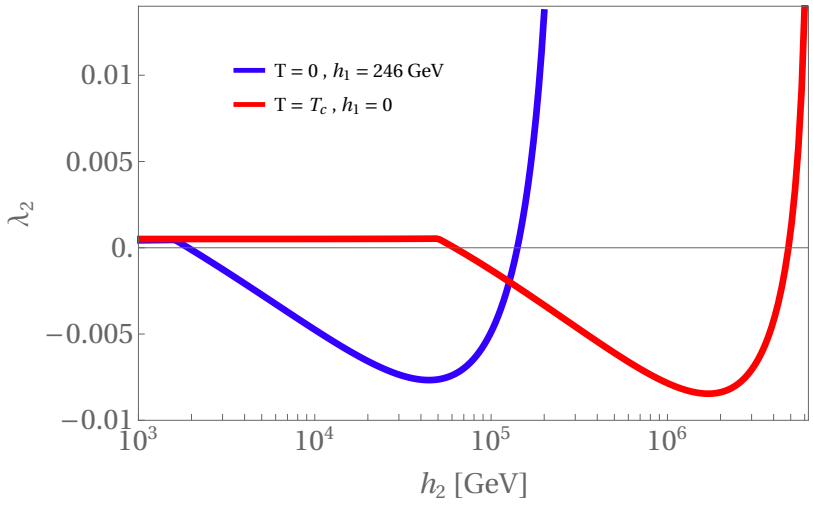

Figure 5.4: Evolution of λ_2 for benchmark M1 at $T = 0$ and $T_c = 3.5$ TeV.

Chapter 6

Conclusion and outlook

6.1 Summary

The main goals of this dissertation are to build renormalizable extensions of SM that predict fermionic-induced EWSNR and study their properties. In Chapter 1, I presented some basic equations to explain why the SM and many extensions of SM generally predict that the EW symmetry was restored in the early universe when the temperature was sufficiently high. The same set of equations also help us to understand why it is possible to have broken EW symmetry at high temperatures in certain scalar extensions of SM. By using similar arguments, we see that it is impossible to have EWSNR if the SM is extended by only adding new fermions with temperature-independent masses in any renormalizable models. These arguments motivate us to construct renormalizable extensions of SM with new fermions that have temperature-dependent masses in Chapter 2.

The Lagrangian of the mass terms and Yukawa interactions related to the new fermions is given in Section 2.1. In general, the new fermions may couple to any $SU(2)_L$ scalar doublets. In this dissertation, two simplest scalar potentials are considered: SM and I2HDM. Their notations are defined in Section 2.2. In Section 2.3, I explained the mechanism for the temperature-dependent fermionic masses and some

qualitative features of the thermal histories of EW symmetry breaking in several scenarios.

At finite temperature, higher loop corrections from the daisy diagrams need to be resummed in order to ensure the perturbative expansion of the effective potential is reliable. As explained in Section 3.1, the daisy contributions can be resummed by adding thermal corrections to the tree-level masses in the effective potential. Besides that, the effective potential can be renormalization-group improved so that it is insensitive to the choice of renormalization scale. In Section 3.2, I described the procedure for calculating the renormalization-group improved effective potential that incorporates the multiple mass scales that exist in our model.

In Section 4.1, I discussed the constraints from the collider experiments, perturbative unitarity bounds, vacuum stability, and thermal equilibrium conditions on the parameter space of our model. In Section 4.2, I presented the numerical calculations of thermal histories for several benchmarks within the allowed parameter space and analyzed the effects of various model parameters on the thermal histories. We found that certain parameter space of the I2HDM+SSD+F0 model predicts strong FOPT. The calculations of the corresponding GW signals and the prospects of detecting these signals are discussed in Chapter 5.

In Section 5.1, I defined the bounce action and true-vacuum bubbles nucleation rate and used them to determine the key parameters of FOPT $(T_n, \beta/H, \alpha)$ that are required for calculating the GWs spectra. In Section 5.2, I described three main production mechanisms (true-vacuum bubbles collisions, sound waves, and magneto-hydrodynamics turbulence) of gravitational waves during the FOPT and summarized the GWs spectra formula. In our case, the sound wave is dominant source of GWs. In Section 5.3, I introduced the signal-to-noise ratio of GW signals and the peak-integrated sensitivity curves of GWs detectors, which help us to assess the discovery potential of GW signal predictions of our models in the future GW experiments.

Finally, I presented several benchmarks that can be probed by BBO and DECIGO.

6.2 Outlook

The mechanism proposed in this thesis may be used to construct models that allow for high-energy EW baryogenesis. In those models, the baryon asymmetry was produced during EWPT at temperatures much higher than the weak scale, hence evade current experiment bounds on electric dipole moment of the electron [85]. The models presented in Chapter 4 do not predict high-energy EW baryogenesis because the EW symmetry was temporarily restored between weak scale ($\approx$ 160 GeV) and the lower temperature limit of the EW broken phase. However, the temporarily restored phase may be removed by adding singlet scalar(s) that interact with the $SU(2)_L$ Higgs doublet. In addition, by choosing the σ field as inflaton (or quintessence), we can construct models that connect the EW physics with inflaton (or dark energy) theories.

Besides the numerical method that is described in Chapter 3, the finite temperature effective potential can also be renormalization-group improved by using RGEs that include temperature as an indepedent scale, for examples, as proposed in [86,87]. It will be interesting to compare the accuracy and effectiveness of different procedures for calculating the higher-order corrections of effective potential at finite temperature.

References

[1] D. A. Kirzhnits and A. D. Linde, "Macroscopic Consequences of the Weinberg Model," *Phys. Lett. B* **42** (1972) 471–474.

[2] S. Weinberg, "Gauge and Global Symmetries at High Temperature," *Phys. Rev. D* **9** (1974) 3357–3378.

[3] K. Kajantie, M. Laine, K. Rummukainen, and M. E. Shaposhnikov, "The Electroweak phase transition: A Nonperturbative analysis," *Nucl. Phys. B* **466** (1996) 189–258, arXiv:hep-lat/9510020.

[4] K. Kajantie, M. Laine, K. Rummukainen, and M. E. Shaposhnikov, "Is there a hot electroweak phase transition at m(H) larger or equal to m(W)?," *Phys. Rev. Lett.* **77** (1996) 2887–2890, arXiv:hep-ph/9605288.

[5] K. Kajantie, M. Laine, K. Rummukainen, and M. E. Shaposhnikov, "A Nonperturbative analysis of the finite T phase transition in SU(2) x U(1) electroweak theory," *Nucl. Phys. B* **493** (1997) 413–438, arXiv:hep-lat/9612006.

[6] F. Csikor, Z. Fodor, and J. Heitger, "Endpoint of the hot electroweak phase transition," *Phys. Rev. Lett.* **82** (1999) 21–24, arXiv:hep-ph/9809291.

[7] M. D'Onofrio and K. Rummukainen, "Standard model cross-over on the lattice," *Phys. Rev. D* **93** no. 2, (2016) 025003, arXiv:1508.07161 [hep-ph].

[8] D. J. H. Chung, A. J. Long, and L.-T. Wang, "125 GeV Higgs boson and electroweak phase transition model classes," *Phys. Rev. D* **87** no. 2, (2013) 023509, arXiv:1209.1819 [hep-ph].

[9] D. Egana-Ugrinovic, "The minimal fermionic model of electroweak baryogenesis," *JHEP* **12** (2017) 064, arXiv:1707.02306 [hep-ph].

[10] A. Angelescu and P. Huang, "Multistep Strongly First Order Phase Transitions from New Fermions at the TeV Scale," *Phys. Rev. D* **99** no. 5, (2019) 055023, arXiv:1812.08293 [hep-ph].

[11] D. Curtin, P. Meade, and C.-T. Yu, "Testing Electroweak Baryogenesis with Future Colliders," *JHEP* **11** (2014) 127, arXiv:1409.0005 [hep-ph].

[12] R. Contino *et al.*, "Physics at a 100 TeV pp collider: Higgs and EW symmetry breaking studies," arXiv:1606.09408 [hep-ph].

[13] C. Caprini *et al.*, "Detecting gravitational waves from cosmological phase transitions with LISA: an update," *JCAP* **03** (2020) 024, arXiv:1910.13125 [astro-ph.CO].

[14] T. Chupp, P. Fierlinger, M. Ramsey-Musolf, and J. Singh, "Electric dipole moments of atoms, molecules, nuclei, and particles," *Rev. Mod. Phys.* **91** no. 1, (2019) 015001, arXiv:1710.02504 [physics.atom-ph].

[15] P. Meade and H. Ramani, "Unrestored Electroweak Symmetry," *Phys. Rev. Lett.* **122** no. 4, (2019) 041802, arXiv:1807.07578 [hep-ph].

[16] T. Biekötter, S. Heinemeyer, J. M. No, M. O. Olea, and G. Weiglein, "Fate of electroweak symmetry in the early Universe: Non-restoration and trapped vacua in the N2HDM," *JCAP* **06** (2021) 018, arXiv:2103.12707 [hep-ph].

[17] M. Carena, C. Krause, Z. Liu, and Y. Wang, "New approach to electroweak symmetry nonrestoration," *Phys. Rev. D* **104** no. 5, (2021) 055016, arXiv:2104.00638 [hep-ph].

[18] M. Quiros, "Finite temperature field theory and phase transitions," in *ICTP Summer School in High-Energy Physics and Cosmology*, pp. 187–259. 1, 1999. arXiv:hep-ph/9901312.

[19] B. W. Lee, C. Quigg, and H. B. Thacker, "Weak Interactions at Very High-Energies: The Role of the Higgs Boson Mass," *Phys. Rev. D* **16** (1977) 1519.

[20] C.-Y. Chen, S. Dawson, and I. M. Lewis, "Exploring resonant di-Higgs boson production in the Higgs singlet model," *Phys. Rev. D* **91** no. 3, (2015) 035015, arXiv:1410.5488 [hep-ph].

[21] R. R. Parwani, "Resummation in a hot scalar field theory," *Phys. Rev. D* **45** (1992) 4695, arXiv:hep-ph/9204216. [Erratum: Phys.Rev.D 48, 5965 (1993)].

[22] P. B. Arnold and O. Espinosa, "The Effective potential and first order phase transitions: Beyond leading-order," *Phys. Rev. D* **47** (1993) 3546, arXiv:hep-ph/9212235. [Erratum: Phys.Rev.D 50, 6662 (1994)].

[23] M. E. Carrington, "The Effective potential at finite temperature in the Standard Model," *Phys. Rev. D* **45** (1992) 2933–2944.

[24] O. Matsedonskyi and G. Servant, "High-Temperature Electroweak Symmetry Non-Restoration from New Fermions and Implications for Baryogenesis," *JHEP* **09** (2020) 012, arXiv:2002.05174 [hep-ph].

[25] T. Cohen, J. Kearney, A. Pierce, and D. Tucker-Smith, "Singlet-Doublet Dark Matter," *Phys. Rev. D* **85** (2012) 075003, arXiv:1109.2604 [hep-ph].

[26] A. Freitas, S. Westhoff, and J. Zupan, "Integrating in the Higgs Portal to Fermion Dark Matter," *JHEP* **09** (2015) 015, arXiv:1506.04149 [hep-ph].

[27] P. Sikivie, L. Susskind, M. B. Voloshin, and V. I. Zakharov, "Isospin Breaking in Technicolor Models," *Nucl. Phys. B* **173** (1980) 189–207.

[28] G. Altarelli and R. Barbieri, "Vacuum polarization effects of new physics on electroweak processes," *Phys. Lett. B* **253** (1991) 161–167.

[29] M. E. Peskin and T. Takeuchi, "Estimation of oblique electroweak corrections," *Phys. Rev. D* **46** (1992) 381–409.

[30] G. C. Branco, P. M. Ferreira, L. Lavoura, M. N. Rebelo, M. Sher, and J. P. Silva, "Theory and phenomenology of two-Higgs-doublet models," *Phys. Rept.* **516** (2012) 1–102, arXiv:1106.0034 [hep-ph].

[31] D. Buttazzo, G. Degrassi, P. P. Giardino, G. F. Giudice, F. Sala, A. Salvio, and A. Strumia, "Investigating the near-criticality of the Higgs boson," *JHEP* **12** (2013) 089, arXiv:1307.3536 [hep-ph].

[32] V. Branchina, E. Messina, and M. Sher, "Lifetime of the electroweak vacuum and sensitivity to Planck scale physics," *Phys. Rev. D* **91** (2015) 013003, arXiv:1408.5302 [hep-ph].

[33] A. Glioti, R. Rattazzi, and L. Vecchi, "Electroweak Baryogenesis above the Electroweak Scale," *JHEP* **04** (2019) 027, arXiv:1811.11740 [hep-ph].

[34] M. Bando, T. Kugo, N. Maekawa, and H. Nakano, "Improving the effective potential: Multimass scale case," *Prog. Theor. Phys.* **90** (1993) 405–418, arXiv:hep-ph/9210229.

[35] J. R. Espinosa, M. Quiros, and F. Zwirner, "On the nature of the electroweak phase transition," *Phys. Lett. B* **314** (1993) 206–216, arXiv:hep-ph/9212248.

[36] M. Bando, T. Kugo, N. Maekawa, and H. Nakano, "Improving the effective potential," *Phys. Lett. B* **301** (1993) 83–89, arXiv:hep-ph/9210228.

[37] K. Symanzik, "Infrared singularities and small distance behavior analysis," *Commun. Math. Phys.* **34** (1973) 7–36.

[38] T. Appelquist and J. Carazzone, "Infrared Singularities and Massive Fields," *Phys. Rev. D* **11** (1975) 2856.

[39] Q.-H. Cao, E. Ma, and G. Rajasekaran, "Observing the Dark Scalar Doublet and its Impact on the Standard-Model Higgs Boson at Colliders," *Phys. Rev. D* **76** (2007) 095011, arXiv:0708.2939 [hep-ph].

[40] E. Lundstrom, M. Gustafsson, and J. Edsjo, "The Inert Doublet Model and LEP II Limits," *Phys. Rev. D* **79** (2009) 035013, arXiv:0810.3924 [hep-ph].

[41] **L3** Collaboration, P. Achard *et al.*, "Search for heavy neutral and charged leptons in e^+e^- annihilation at LEP," *Phys. Lett. B* **517** (2001) 75–85, arXiv:hep-ex/0107015.

[42] M. D. Schwartz, *Quantum Field Theory and the Standard Model*. Cambridge University Press, 3, 2014.

[43] S. Kanemura and K. Yagyu, "Unitarity bound in the most general two Higgs doublet model," *Phys. Lett. B* **751** (2015) 289–296, arXiv:1509.06060 [hep-ph].

[44] A. Belyaev, G. Cacciapaglia, I. P. Ivanov, F. Rojas-Abatte, and M. Thomas, "Anatomy of the Inert Two Higgs Doublet Model in the light of the LHC and non-LHC Dark Matter Searches," *Phys. Rev. D* **97** no. 3, (2018) 035011, arXiv:1612.00511 [hep-ph].

[45] L. Di Luzio, J. F. Kamenik, and M. Nardecchia, "Implications of perturbative unitarity for scalar di-boson resonance searches at LHC," *Eur. Phys. J. C* **77** no. 1, (2017) 30, arXiv:1604.05746 [hep-ph].

[46] L. Delle Rose, C. Marzo, and A. Urbano, "On the fate of the Standard Model at finite temperature," *JHEP* **05** (2016) 050, arXiv:1507.06912 [hep-ph].

[47] E. W. Kolb and M. S. Turner, *The Early Universe*, vol. 69. 1990.

[48] N. Christensen, "Stochastic Gravitational Wave Backgrounds," *Rept. Prog. Phys.* **82** no. 1, (2019) 016903, arXiv:1811.08797 [gr-qc].

[49] S. W. Hawking, I. G. Moss, and J. M. Stewart, "Bubble Collisions in the Very Early Universe," *Phys. Rev. D* **26** (1982) 2681.

[50] M. S. Turner, E. J. Weinberg, and L. M. Widrow, "Bubble nucleation in first order inflation and other cosmological phase transitions," *Phys. Rev. D* **46** (1992) 2384–2403.

[51] **Particle Data Group** Collaboration, P. A. Zyla *et al.*, "Review of Particle Physics," *PTEP* **2020** no. 8, (2020) 083C01.

[52] C. G. Callan, Jr. and S. R. Coleman, "The Fate of the False Vacuum. 2. First Quantum Corrections," *Phys. Rev. D* **16** (1977) 1762–1768.

[53] A. D. Linde, "Decay of the False Vacuum at Finite Temperature," *Nucl. Phys. B* **216** (1983) 421. [Erratum: Nucl.Phys.B 223, 544 (1983)].

[54] V. Guada, M. Nemevšek, and M. Pintar, "FindBounce: Package for multi-field bounce actions," *Comput. Phys. Commun.* **256** (2020) 107480, arXiv:2002.00881 [hep-ph].

[55] L. P. Csernai and J. I. Kapusta, "Nucleation of relativistic first order phase transitions," *Phys. Rev. D* **46** (1992) 1379–1390.

[56] I. Affleck, "Quantum Statistical Metastability," *Phys. Rev. Lett.* **46** (1981) 388.

[57] D. Croon, O. Gould, P. Schicho, T. V. I. Tenkanen, and G. White, "Theoretical uncertainties for cosmological first-order phase transitions," *JHEP* **04** (2021) 055, arXiv:2009.10080 [hep-ph].

[58] G. D. Moore and K. Rummukainen, "Electroweak bubble nucleation, nonperturbatively," *Phys. Rev. D* **63** (2001) 045002, arXiv:hep-ph/0009132.

[59] P. B. Arnold, D. T. Son, and L. G. Yaffe, "Effective dynamics of hot, soft nonAbelian gauge fields. Color conductivity and log(1/alpha) effects," *Phys. Rev. D* **59** (1999) 105020, arXiv:hep-ph/9810216.

[60] P. B. Arnold and L. G. Yaffe, "Nonperturbative dynamics of hot nonAbelian gauge fields: Beyond leading log approximation," *Phys. Rev. D* **62** (2000) 125013, arXiv:hep-ph/9912305.

[61] P. B. Arnold, D. Son, and L. G. Yaffe, "The Hot baryon violation rate is O (alpha-w**5 T**4)," *Phys. Rev. D* **55** (1997) 6264–6273, arXiv:hep-ph/9609481.

[62] T. Konstandin, G. Nardini, and M. Quiros, "Gravitational Backreaction Effects on the Holographic Phase Transition," *Phys. Rev. D* **82** (2010) 083513, arXiv:1007.1468 [hep-ph].

[63] T. Konstandin and G. Servant, "Cosmological Consequences of Nearly Conformal Dynamics at the TeV scale," *JCAP* **12** (2011) 009, arXiv:1104.4791 [hep-ph].

[64] T. W. B. Kibble and A. Vilenkin, "Phase equilibration in bubble collisions," *Phys. Rev. D* **52** (1995) 679–688, arXiv:hep-ph/9501266.

[65] E. W. Kolb and A. Riotto, "Preheating and symmetry restoration in collisions of vacuum bubbles," *Phys. Rev. D* **55** (1997) 3313–3317, arXiv:astro-ph/9602095.

[66] R. Watkins and L. M. Widrow, "Aspects of reheating in first order inflation," *Nucl. Phys. B* **374** (1992) 446–468.

[67] J. R. Espinosa, T. Konstandin, J. M. No, and G. Servant, "Energy Budget of Cosmological First-order Phase Transitions," *JCAP* **06** (2010) 028, arXiv:1004.4187 [hep-ph].

[68] A. Kosowsky, M. S. Turner, and R. Watkins, "Gravitational radiation from colliding vacuum bubbles," *Phys. Rev. D* **45** (1992) 4514–4535.

[69] A. Kosowsky and M. S. Turner, "Gravitational radiation from colliding vacuum bubbles: envelope approximation to many bubble collisions," *Phys. Rev. D* **47** (1993) 4372–4391, arXiv:astro-ph/9211004.

[70] J. Ignatius, K. Kajantie, H. Kurki-Suonio, and M. Laine, "The growth of bubbles in cosmological phase transitions," *Phys. Rev. D* **49** (1994) 3854–3868, arXiv:astro-ph/9309059.

[71] M. Hindmarsh, S. J. Huber, K. Rummukainen, and D. J. Weir, "Numerical simulations of acoustically generated gravitational waves at a first order phase transition," *Phys. Rev. D* **92** no. 12, (2015) 123009, arXiv:1504.03291 [astro-ph.CO].

[72] C. Caprini, R. Durrer, and G. Servant, "The stochastic gravitational wave background from turbulence and magnetic fields generated by a first-order phase transition," *JCAP* **12** (2009) 024, arXiv:0909.0622 [astro-ph.CO].

[73] A. Roper Pol, S. Mandal, A. Brandenburg, T. Kahniashvili, and A. Kosowsky, "Numerical simulations of gravitational waves from early-universe turbulence," *Phys. Rev. D* **102** no. 8, (2020) 083512, arXiv:1903.08585 [astro-ph.CO].

[74] D. T. Son, "Magnetohydrodynamics of the early universe and the evolution of primordial magnetic fields," *Phys. Rev. D* **59** (1999) 063008, arXiv:hep-ph/9803412.

[75] A. Brandenburg, T. Kahniashvili, S. Mandal, A. Roper Pol, A. G. Tevzadze, and T. Vachaspati, "Evolution of hydromagnetic turbulence from the electroweak phase transition," *Phys. Rev. D* **96** no. 12, (2017) 123528, arXiv:1711.03804 [astro-ph.CO].

[76] G. Barenboim and W.-I. Park, "Gravitational waves from first order phase transitions as a probe of an early matter domination era and its inverse problem," *Phys. Lett. B* **759** (2016) 430–438, arXiv:1605.03781 [astro-ph.CO].

[77] C. Caprini *et al.*, "Science with the space-based interferometer eLISA. II: Gravitational waves from cosmological phase transitions," *JCAP* **04** (2016) 001, arXiv:1512.06239 [astro-ph.CO].

[78] C. J. Moore, R. H. Cole, and C. P. L. Berry, "Gravitational-wave sensitivity curves," *Class. Quant. Grav.* **32** no. 1, (2015) 015014, arXiv:1408.0740 [gr-qc].

[79] C. Caprini, R. Durrer, and X. Siemens, "Detection of gravitational waves from the QCD phase transition with pulsar timing arrays," *Phys. Rev. D* **82** (2010) 063511, arXiv:1007.1218 [astro-ph.CO].

[80] K. Schmitz, "New Sensitivity Curves for Gravitational-Wave Signals from Cosmological Phase Transitions," *JHEP* **01** (2021) 097, arXiv:2002.04615 [hep-ph].

[81] B. Allen, "The Stochastic gravity wave background: Sources and detection," in *Les Houches School of Physics: Astrophysical Sources of Gravitational Radiation*, pp. 373–417. 4, 1996. arXiv:gr-qc/9604033.

[82] B. Allen and J. D. Romano, "Detecting a stochastic background of gravitational radiation: Signal processing strategies and sensitivities," *Phys. Rev. D* **59** (1999) 102001, arXiv:gr-qc/9710117.

[83] M. Breitbach, J. Kopp, E. Madge, T. Opferkuch, and P. Schwaller, "Dark, Cold, and Noisy: Constraining Secluded Hidden Sectors with Gravitational Waves," *JCAP* **07** (2019) 007, arXiv:1811.11175 [hep-ph].

[84] Y. Cheng and W. Liao, "Fate of the false vacuum in a singlet-doublet fermion extension model with RG-improved effective action," *Phys. Rev. D* **101** no. 5, (2020) 055038, arXiv:1909.11941 [hep-ph].

[85] **ACME** Collaboration, V. Andreev *et al.*, "Improved limit on the electric dipole moment of the electron," *Nature* **562** no. 7727, (2018) 355–360.

[86] S.-B. Liao and M. Strickland, "Renormalization group approach to field theory at finite temperature," *Phys. Rev. D* **52** (1995) 3653–3671, arXiv:hep-th/9501137.

[87] H. Nakkagawa and H. Yokota, "RG improvement of the effective potential at finite temperature," *Mod. Phys. Lett. A* **11** (1996) 2259–2269.

[88] J. R. Espinosa, M. Losada, and A. Riotto, "Symmetry nonrestoration at high temperature in little Higgs models," *Phys. Rev. D* **72** (2005) 043520, arXiv:hep-ph/0409070.

[89] M. J. Ramsey-Musolf, P. Winslow, and G. White, "Color Breaking Baryogenesis," *Phys. Rev. D* **97** no. 12, (2018) 123509, arXiv:1708.07511 [hep-ph].

[90] D. Cutting, M. Hindmarsh, and D. J. Weir, "Vorticity, kinetic energy, and suppressed gravitational wave production in strong first order phase transitions," *Phys. Rev. Lett.* **125** no. 2, (2020) 021302, arXiv:1906.00480 [hep-ph].

[91] M. Srednicki, R. Watkins, and K. A. Olive, "Calculations of Relic Densities in the Early Universe," *Nucl. Phys. B* **310** (1988) 693.

Appendix A

Mass matrix and mixing angles of SSD model

The mass terms of SSD model (eq.(2.1)) can be written as

$$\mathcal{L}^{i}_{\text{SSD-mass}} = \sum_{f=N,E} \overline{F^f_L} M_{ff'}(h,s) F^f_R + \text{h.c.}\,, \tag{A.1}$$

where

$$F^f_{L,R} \equiv \begin{bmatrix} f' \\ f \end{bmatrix}_{L,R}, \quad M_{ff'}(h,s) \equiv \begin{bmatrix} m_{f'}(s) & m_2(h) \\ m_1(h) & m_L(s) \end{bmatrix} \quad (f = N, E)\,,$$
$$m_i(h) \equiv \frac{1}{\sqrt{2}} y_{ff'i} h \quad (i = 1, 2)\,, \quad m_X(s) \equiv m_{X0} + y_X s \quad (X = f', L)\,.$$

$M_{ff'}$ can be diagonalized via bi-unitary transformations of $F^f_{L,R}$:

$$F^f_{L,R} = U^f_{L,R} \begin{bmatrix} f_1 \\ f_2 \end{bmatrix}_{L,R}, \quad U^f_{L,R} = \begin{bmatrix} \cos\theta^f_{L,R} & \sin\theta^f_{L,R} \\ -\sin\theta^f_{L,R} & \cos\theta^f_{L,R} \end{bmatrix}, \tag{A.2}$$

$$\begin{bmatrix} m_{f1} & 0 \\ 0 & m_{f2} \end{bmatrix} = U^{f\dagger}_L M_{ff'} U^f_R\,. \tag{A.3}$$

f_1, f_2 are mass eigenstates and their eigenvalues m_{f1}, m_{f2} are given by eq.(2.3-2.4). The mixing angles $\theta^f_{L,R}$ satisfy

$$\tan 2\theta^f_L = \frac{2(m_{f'} m_1 + m_L m_2)}{m_L^2 - m_{f'}^2 + m_1^2 - m_2^2}\,. \tag{A.4}$$

$\tan 2\theta^f_R$ is same as eq.(A.4), except $1 \leftrightarrow 2$. Now we can use $U^f_{L,R}$ to obtain the yukawa

coupings between σ and the mass eigenstates (f_1, f_2) of the new fermions:

$$y_{f_i f_j \sigma} = \left(U_L^{f\dagger} \partial_\sigma M_{ff'}(H^0, \sigma) U_R^f \right)_{ij} . \tag{A.5}$$

$$y_{f_1 f_1 \sigma} = y_{f'} \cos\theta_L^f \cos\theta_R^f + y_L \sin\theta_L^f \sin\theta_R^f . \tag{A.6}$$

$$y_{f_2 f_2 \sigma} = y_L \cos\theta_L^f \cos\theta_R^f + y_{f'} \sin\theta_L^f \sin\theta_R^f . \tag{A.7}$$

In our numerical studies, $y_{ff'1} = y_{ff'2}$, thus $\theta_L^f = \theta_R^f$. Also, when $m_L(s) - m_{f'}(s) \gg m_i(h)$, the mixing angle is small, thus

$$\theta_L^f = \theta_R^f \approx \frac{m_1}{m_L - m_{f'}} , \tag{A.8}$$

$$y_{f_1 f_1 \sigma} \approx y_{f'} + (y_L - y_{f'}) \theta_L^{f2} , \tag{A.9}$$

$$y_{f_2 f_2 \sigma} \approx y_L + (y_{f'} - y_L) \theta_L^{f2} . \tag{A.10}$$

Appendix B

Calculation of $D_{f\sigma}$

In this appendix, the (leading order) interaction rate of $f_i f_i \to \sigma\sigma$ ($f \in \{N, E\}$, $i \in \{1, 2\}$) at finite temperatures will be calculated without assuming $m_{fi} \ll T$. I will follow the definitions and procedures given in [91]. At $T = 0$, the product of cross section and relative velocity is

$$\sigma v_{\rm rel} = \frac{w(s)}{E_1 E_2}\,, \quad w(s) \equiv \frac{1}{4}\int dLIPS\,|\mathcal{M}|^2\,, \quad s \equiv -(p_1+p_2)^2\,, \tag{B.1}$$

where $dLIPS$ is the usual Lorentz-invariant phase space measure and $\mathcal{M}$ is the invariant scattering matrix elememnt. However, T is high in the early universe and the thermal distributions of interacting particles need to be included by taking the thermal average of $\sigma v_{\rm rel}$:

$$\langle \sigma v_{\rm rel} \rangle = \frac{1}{n_i^2}\int d^3p_1 d^3p_2\, \mathcal{N}_i(E_1)\mathcal{N}_i(E_2)\frac{w(s)}{E_1 E_2}\,, \tag{B.2}$$

where $n_i = \int d^3p\, \mathcal{N}_i(E)$. Here, I am interest in $m_{fi}/T > 1.5$, so the thermal distributions are well approximated by Maxwell-Boltzmann distribution $\mathcal{N}_i(E) = \frac{d_i}{(2\pi)^3} e^{-E/T}$. Since the integrand of eq.(B.1) is exponential suppressed by $e^{-(E_1+E_2)/T}$ and m_{fi}/T is large, it is justified to expand the integrand around $s = 4m_{fi}^2$. Small

expansion around $s = 4m_{fi}^2$ gives

$$w(\tilde{s}) \approx (y_{f_i f_i \sigma}^2/(4\pi))^2 \, F(\tilde{s}) \,, \tag{B.3}$$

$$\tilde{s} \equiv s/(4m_{fi}^2) \,, \quad F(\tilde{s}) = 2\pi[3\tilde{s} - (25/16)(\tilde{s} - 1/4)^{-1} - 9/4] \,. \tag{B.4}$$

It is also useful to use dimensionless variables in the integrations of $\langle \sigma v_{\rm rel} \rangle$ (see eq.(26) in [91]) and n_i, so that the m_{fi}/T and temperature dependencies of $\Gamma(f_i f_i \to \sigma\sigma) = n_i \langle \sigma v_{\rm rel} \rangle$ become transparent. The result is

$$\Gamma(f_i f_i \to \sigma\sigma) = T(y_{f_i f_i \sigma}^2/(4\pi))^2 \, D_{f\sigma}(m_{fi}/T) \,, \tag{B.5}$$

$$D_{f\sigma}(r) = \frac{d_i \, r e^{-2r}}{2\pi^2 \tilde{n}(r)} \int_0^\infty dy_1 dy_2 \left(y_1 + \frac{y_1^2}{2r}\right)^{1/2} \left(y_2 + \frac{y_2^2}{2r}\right)^{1/2} e^{-(y_1+y_2)} \int_{-1}^{1} d\cos\theta F(\tilde{s}) \,, \tag{B.6}$$

$$\tilde{n}(r) = \int_r^\infty dy \frac{y(y^2 - r^2)^{1/2}}{e^y + 1} \,, \tag{B.7}$$

$$\tilde{s} = 1 + \frac{y_1 + y_2}{2r} + \frac{y_1 y_2}{2r^2} - \frac{1}{r}\left(y_1 + \frac{y_1^2}{2r}\right)^{1/2} \left(y_2 + \frac{y_2^2}{2r}\right)^{1/2} \cos\theta \,. \tag{B.8}$$

Thus, eq.(B.5) and the thermal equilibrium condition (4.11) imply eq.(4.19). $D_{f\sigma}$ is evaluated numerically and the result is shown in Fig. 4.1.